e-ISSN : 2716-1285
ISSN : 2714-9722

JOURNAL OF MATERIALS PROCESSING & CHARACTERIZATION

Jointly Published by:

Department of Mechanical and Industrial Engineering, Faculty of Engineering, Universitas Gadjah Mada

Centre for Innovation of Medical Equipment and Devices (CIMEDs) Faculty of Engineering, Universitas Gadjah Mada

Volume 1, Number 1, June 2020

e-ISSN : 2716-1285
ISSN : 2714-9722

JOURNAL OF MATERIAL PROCESSING AND CHARACTERIZATION

Volume 1, Number 1, June 2020

Table Of Contents

PREFACE

Welcome to the inaugural issue of Journal of Materials Processing and Characterization: a peer-refereed academic journal. With its broad scope bridging (yet not limited to) all the research topics related to the processing (such as material preparations, fabrication techniques, post-processing treatments) and characterizations (such as novel methods for characterization, experimental testing and numerical analyses) of metals, polymers, ceramics and composites. This journal will publish mostly research papers: experimental, computational and theoretical.

The inaugural issue consists of seven papers. The papers report about characterization (mechanical, physical, chemical and microstructural) and processing (powder metallurgy, polishing, composite process, welding, and solidification).

Using the journal inauguration as an occasion, I would like to thank many people who created the opportunity for the journal to be born and who made it happen. The list includes all current Editorial Board, reviewers and administration team. The last, but not the least my greatest thanks goes to Department of Mechanical and Industrial Engginering, Faculty of Engineering Gadjah Mada University and Centre for Innovation of Medical Equipment and Devices (CIMEDs) for supporting this journal.

Suyitno
Editor-in-chief

EDITORIAL TEAM

Managed and published by:
Department of Mechanical and Industrial Engineering, Faculty of Engineering, Universitas Gadjah Mada and Centre for Innovation of Medical Equipment and Devices (CIMEDs) Faculty of Engineering, Universitas Gadjah Mada

Website: https://jurnal.ugm.ac.id/jmpc
email: jmpc@ugm.ac.id

JOURNAL OF MATERIALS PROCESSING & CHARACTERIZATION

Compressive Strength and Thermal Conductivity of Porous Mullite Ceramics

M. W. Wildan*
F. Marpaung

Department of Mechanical and Industrial Engineering, Faculty of Engineering, Universitas Gadjah Mada. Jl. Grafika 2, Yogyakarta 55281, Indonesia

Email:
*m_wildan@ugm.ac.id

Keywords
kaolin, mullite, dry yeast powder, porosity, compressive strength, thermal conductivity, PFA (pore-forming agent).

Abstract
Porous ceramics are a form of ceramic material with widespread applications, such as filters, isolators, and acoustics. This research aimed to investigate the compressive strength and thermal conductivity of porous mullite ceramics ($3Al_2O_3.2SiO_2$ or $Si_2Al_6O_{13}$) produced using dry yeast powder as a PFA (pore-forming agent). Kaolin powder ($Al_2O_3.2SiO_4.2H_2O$ or $Al_2Si_2O_5(OH)_4$) was used as a raw material for producing mullite ceramics. Kaolin powder and dry yeast powder were mixed at a variety of dry yeast powder weight fractions: 0%, 5%, 10%, 15%, 20%, and 25%. The composition was mixed using Turbula Mixer for 1 hour. The cylindrical green body (diameters of 12 mm, 15 mm, and 30 mm) of every constituent was formed by the uniaxial pressing method at 10 MPa. Monolithic kaolin was sintered at variable temperatures (1,100°C, 1,200 °C, 1,300 °C, 1,400 °C, 1,450 °C) for 2 hours then subjected to several tests for its density. From the bulk density tests, it was found that the optimum temperature for 2-hour sintering was 1,450 °C. This temperature was then used for the sintering process of the kaolin specimens which contained dry yeast powder. Testing was performed on the microstructure, bulk density, burning waste in mass and volume, compressive strength, and thermal conductivity. According to the literature, kaolin will transform into mullite ($3Al_2O_3.2SiO_2$ atau $Si_2Al_6O_{13}$) and cristobalite (SiO_2) at 1,450 °C. It was found that with the increase in the content of dry yeast powder as PFA in the mixture with kaolin, the bulk density decreased (from 2.44 gr/ cm^3 to 1.521 gr/ cm^3), the porosity increased (from 23.77% to 52.48%), the compressive strength decreased (from 38.04 MPa to 4.51 MPa), and the thermal conductivity decreased (from 3.76 W/m°C to1.34 W/m°C), each from yeast powder content 0% to 25%.

Volume 1, Number 1, 2020, 1-7
DOI: http://dx.doi.org/10.22146/jmpc.v1i1.51410
e-ISSN: 2716-1285, ISSN: 2714-9722

1. Introduction

Engineering ceramics are usually more advantageous than engineering materials of any other types in a variety of aspects, including high strength at high temperatures, high modulus of elasticity, high hardness, wear resistance, low coefficient of thermal expansion, and relatively low density (Barsoum, 2003). One of the ceramic materials constantly produced is porous ceramic. Porous ceramics have vast applications, for example, in membranes, filters, biomaterials, thermal insulators, and acoustics. As a result, production of porous ceramics with controlled microstructure in terms of porosity, pore size, and pore space topology has become an important, intriguing topic in the last few decades.

Porous ceramics can lower thermal conductivity and at the same time increase thermal resistance, or in other words, they are suited for use as thermal insulators (Barsoum, 2003).

The porous ceramics fabrication methods developing at the present include the sol-gel process (for nanometer-scale pores and high levels of porosity) (Liu and Chen, 2014), the polymer foam-based template method (for big-sized pores and high levels of porosity), the biomimetic method (using pyrolyzed Wood templates), the ceramic hollow spheres method (e.g., alumina microballoons), and the sacrifical (pyrolyzable) pore-forming agent method (PFA) (using organic materials or biopolymers burnable during sintering). Some of the materials which have been developed into forming agents are polymethyl methacrylate (Chen et al., 2005), rice starch and potato starch (Gregorova et al., 2006), poppy seed (Gregorova and Pabst, 2006), rice husk (Manap and Jais, 2009), corn starch (Wildan et al., 2009), and coconut shell charcoal (Sandra et al., 2014). Some formation methods and porous ceramics' properties tests have also been discussed in detail by Hammel et al. (2014).

Mullite ceramics ($3Al_2O_3.2SiO_2$) are engineering ceramic materials with wide applications, including, for example, refractories, whiteware, and structures. Mullite has a melting point of 1,830 °C in the air, density of 3.16 g/cm^3, Young's modulus of 50–220 GPa, fracture toughness of 2.6 MPa.m^{0,5}, and thermal conductivity of around 6.0 W/ m^{o}C (Kingon and Davis, 2000). Besides, mullite ceramics also have other good properties, namely high temperature stability, relatively low creep rate, low coefficient of thermal expansion, and low thermal conductivity, hence applied for thermal insulation (Chen and Tuan, 2001). The low thermal conductivity can be intensified by making the mullite material porous (Barsoum, 2003). Pores can lower the thermal conductivity of a solid as conductivity in vacuum is lower than in solid matters.

Research in the field of porous ceramics is still open to grow in topics of types of ceramic materials, pore-making methods, measured properties, applications, among others. This research aimed to figure out the compressive strength and thermal conductivity of porous mullite ceramics manufactured using dry yeast powder as a PFA (pore-forming agent). Kaolin powder was used as the raw material to make the mullite ceramics. Ceramic materials have a wide array of applications and relatively low sintering temperatures. The kaolin ceramic material is a refractory material with superiority in physical, mechanical, and thermal properties like being lightweight, hard, resistant to high temperatures, strong, and so forth.

2. Materials and Methods

The materials used in this research were kaolin powder (from Sigma Aldrich, serial number: 03584) and active dry yeast powder. The particulate size distribution was measured using dry yeast powder by screening. The kaolin powder was mixed with the dry yeast powder at a variety of weight fractions: 0, 5, 10, 10, 15, 20, and 25% dry yeast powder. The composition was mixed together with Turbula Mixer for 1 hour in an alcohol medium. The green body specimens

were made by applying uniaxial pressure at 10 MPa. In making the green body specimens, a little bit of molasses was added as a binder to assist in the forming process. Three sizes of cylindrical green body specimens were applied: diameter of 12 mm, thickness of about 10 mm; diameter of 15 mm, thickness of about 5 mm, and diameter of 30 mm, thickness of about 8 mm. The 15-mm-diameter cylindrical specimen was subjected to density tests, the 12-mm-diameter cylindrical specimen to compressive strength tests, and the 30-mm-diameter cylindrical specimen to thermal conductivity tests. The 15-mm-diameter cylindrical green body specimen was sintered at variable temperatures (1,100 °C, 1,200 °C, 1,300 °C, 1,400 °C, and 1,450 °C) and heating rate of 7 °C/minute, maintained for 2 hours. The sintering product was then subjected to the density tests by Archimedes's method in a mercury medium. Based on the density data, it was found that sintering at 1,450 °C resulted in optimum density. Thus, the temperature 1,450 °C was selected as the sintering temperature to be applied to the rest of the specimens. All of the green body specimens were then sintered by pressureless sintering in the air at 1,450 °C and heating rate of 7 °C /minute, maintained for 2 hours. The bulk density of the sintered specimens was subjected to some tests by Archiedes's method. The compressive strength tests were performed on the 12-mm-diameter cylindrical specimen, while the thermal conductivity tests on the 30-mm-diameter cylindrical specimen. The microstructure was observed under a scanning electron microscope (SEM).

3. Results and Discussion

The results of the measurement of yeast powder particulate sizes by the screening method is displayed in Figure 1. The varying particulate sizes from 0.297 mm through 1.68 mm were distributed (percent weight) as follows: 2% was sized 1.68 mm, 16% was sized 1.19 mm, 23% was sized 0.841 mm, 47% was sized 0.595 mm, and 11% was sized 0.297 mm. Figures 2 and 3 display the particulate shapes of the dry yeast powder and the kaolin powder, respectively. The dry yeast powder particles were rounded and nearly spherical, while the kaolin powder particles flat and layered.

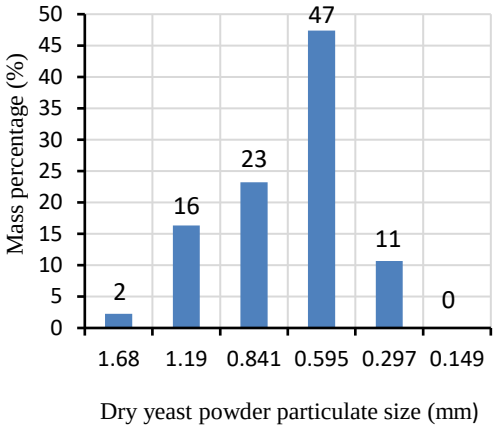

Figure 1. Distribution of dry yeast powder particulate sizes

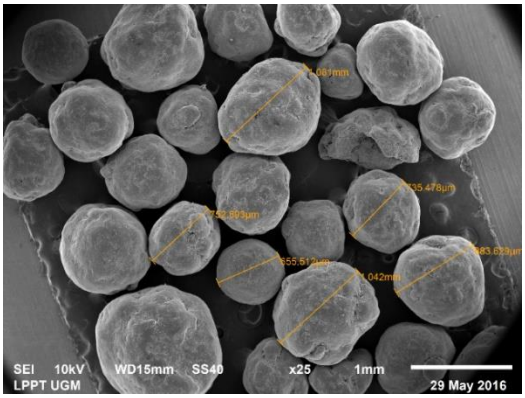

Figure 2. SEM image of dry yeast powder

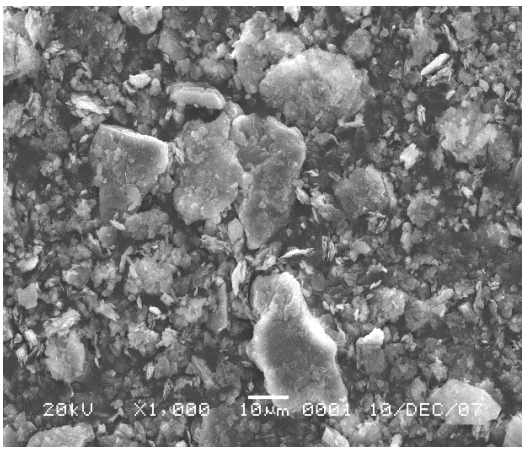

Figure 3. Kaolin powder

The effect of kaolin sintering temperature on the bulk density of the sintering product is shown in Figure 4. As with the sintering process in general, the higher the sintering temperature, the tighter the bond between particles, causing the bulk density and the relative density to also rise. Figure 4 shows that at temperatures between 1,300°C and 1,450 °C, no significant change in density took place. For this reason, 1,450 °C was selected as the sintering temperature for kaolin.

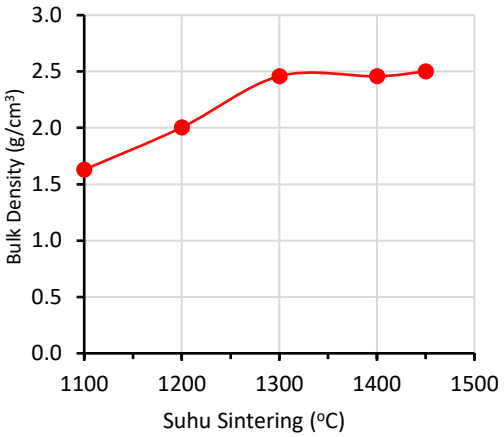

Figure 4. Bulk density of sintered monolithic kaolin as a function of sintering temperature

During a sintering process, kaolin is undergoing a phase transformation into mullite and cristoballite through a number of stages (lee and Reinforth, 1994; Wildan et al., 2009). The transformation stages are as follows:

Kaolin ($Al_2O_3.SiO_2.2H_2O$) undergoes an endothermic dehydroxylation reaction starting at 550–600 °C into metakaolin ($Al_2Si_2O_7$) until it releases a hydroxyl (-OH) ion at 900 °C.

$$2Al_2Si_2O_5(OH)_4 \rightarrow 2Al_2Si_2O_7 + 4H_2O \quad (1)$$

The heating carries on, and at 925–950 °C metakaolin transforms into defect aluminum-silicon spinel:

$$2Al_2Si_2O_7 \rightarrow Si_3Al_4O_{12} + SiO_2 \quad (2)$$

At 1,050 °C, spinel undergoes nucleation and transforms into mullite and cristobalite (high crystalline cristobalite):

$$3Si_3Al_4O_{12} \rightarrow 2Si_2Al_6O_{13} + 5SiO_2 \quad (3)$$

From the sintering process mullite and cristobalite were produced. Based on literature, the theoretical density of mullite is 3.05 g/cm³ (mullite data, webmineral.com), and cristoballite 2.27 g/cm³ (christobalite data, webmineral.com). Following the theoretical density data and the transformation of kaolin into mullite and cristobalite during the sintering precess, the theoretical density of the sintering products was estimated or calculated using the rule of mixture as 2.71 g/cm³. Figure 5 shows the relative density of the kaolin sintering products of mullite and cristoballite. The specimens sintered at 1,450 °C generated relative density of over 95%.

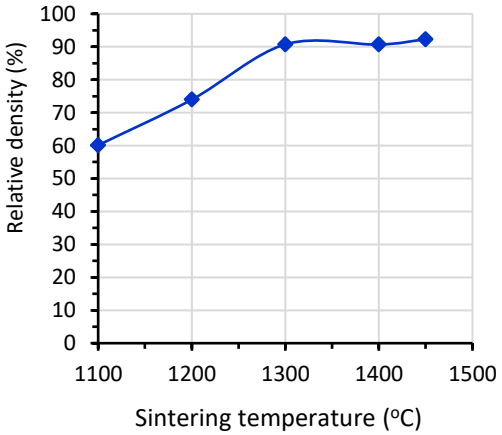

Figure 5. Relative density of sintered monolithic kaolin as a function of sintering temperature

Based on this phenomenon, the mass reduction during the sintering process could be estimated. For monolithic kaolin, mass reduction was be calculated theoretically based on the change from an initial condition as kaolin ($Al_2O_3.SiO_2.2H_2O$) into mullite and cristobalite. The amount of the theoretical mass reduction in the kaolin specimens which contained dry yeast powder was theoretically calculated based on kaolin mass reduction

from the transformation into mullite and cristobalite and on the mass reduction from the firing of the dry yeast powder corresponding to the weight fractions. The theoretical and actual mass reductions can be seen in Figure 6. The difference between the actual and theoretical mass reductions was presumably caused by the presence of molasses which were added as binders during the green body formation and of the presence of moisture in the green body. The mass reductions of the specimens over the sintering process increased with the increase in dry yeast powder weight fraction.

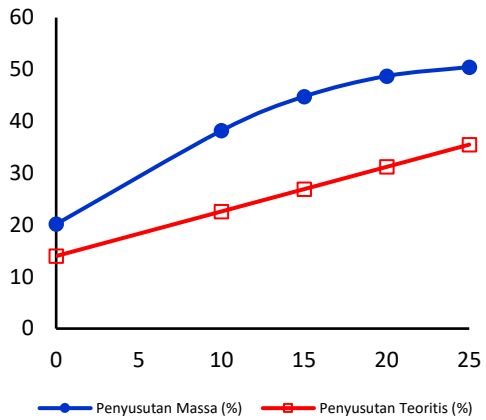

Figure 6. Effect of dry yeast powder weight fraction on mass reduction during the porous mullite ceramics sintering

Over the sintering process course, the dry yeast powder was fired, leaving voids in the sintered specimens. With the increase in the dry yeast powder weight fractions the sintered specimens' porosity also increased. Porosity is a ratio of the voids' volume to the specimen's total volume. Porosity can be estimated based on the bulk density and theoretical density as follows (Wildan et al., 2009):

$$porosity = 1 - \frac{\text{bulk density}}{theoretical\ density} \qquad (4)$$

The porosity of the sintered specimens increased with the increase in the dry yeast powder weight fraction as can be observed in Figure 7. Porosity rose from 9.98 ± 3.52% in specimen with 0% active dry yeast powder weight fraction into 43.87 ± 4.80% in one with 25% active dry yeast powder weight fraction.

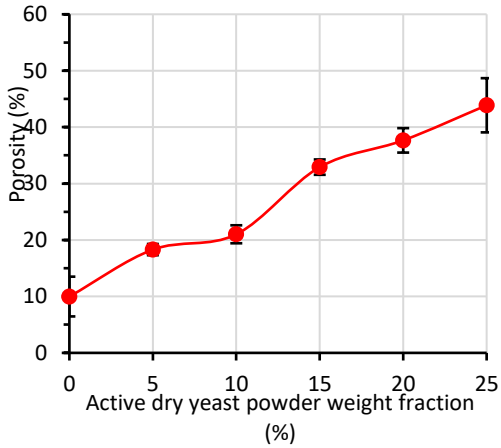

Figure 7. Effect of dry yeast powder weight fraction on the porosity of the porous mullite ceramics

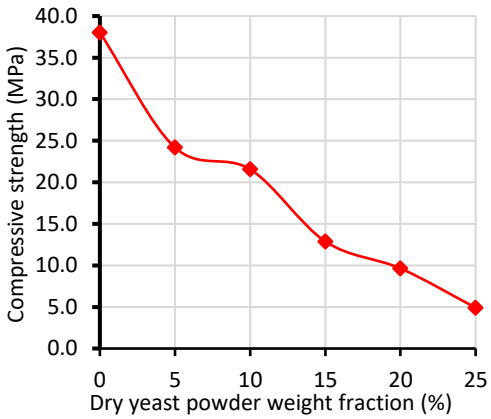

Figure 8. Effect of dry yeast powder weight fraction on the compressive strength of the porous mullite ceramics

Figure 8 demonstrates the compressive strength of the sintered specimens as a function of dry yeast powder weight fraction. The compressive strength decreased with the increase in the dry yeast powder weight fraction. The compressive strength fell from 38.04±5.02 MPa in specimen with 0% dry yeast powder weight

fraction into 4.92±1.81 MPa in one with 25% dry yeast powder weight fraction. This compressive strength drop was attributed to the rise of porosity, where porosity caused stress concentration and reduced the load-receiving area (Barsoum, 2003).

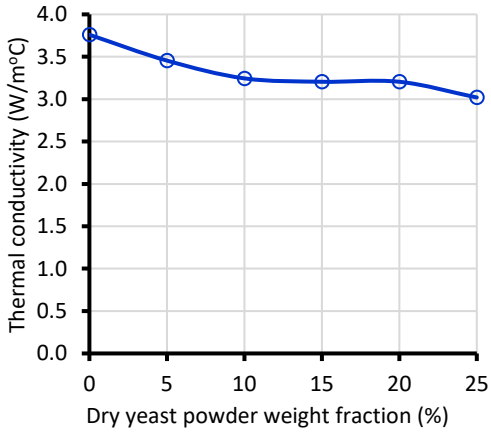

Figure 9. Effect of dry yeast powder weight fraction on the thermal conductivity of the porous mullite ceramics

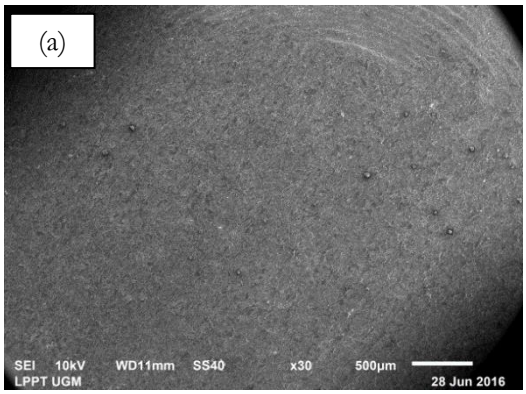

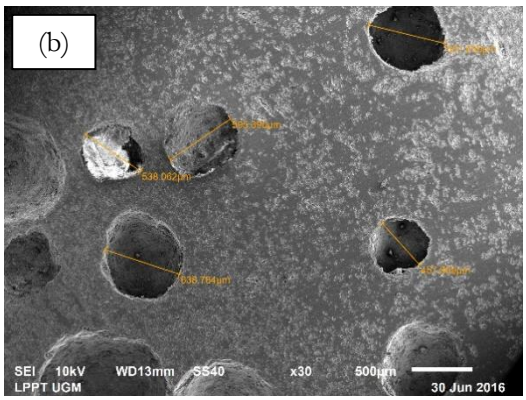

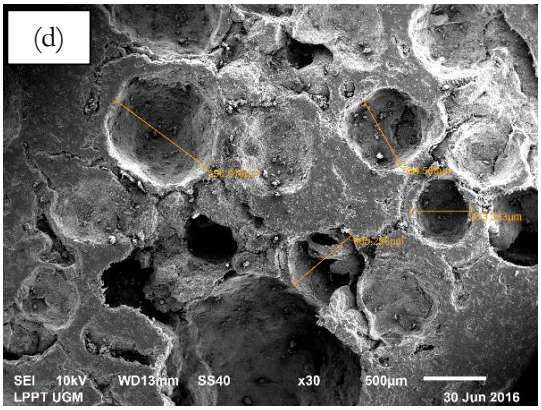

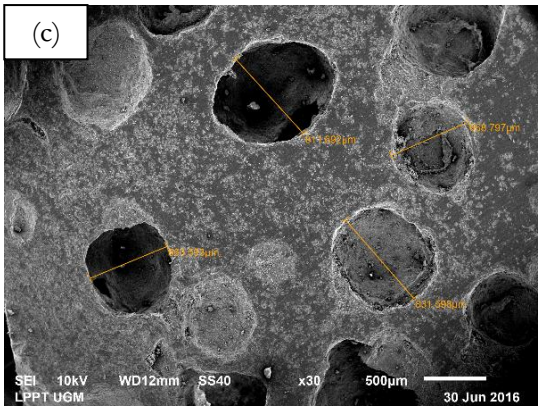

Figure 10. Specimens' microstructures as SEM-imaged for dry yeast powder weight fractions (a) 0%, (b) 10%, (c) 15%, and (d) 25%.

Figure 9 indicates the effect of the thermal conductivity of the sintered specimens on the dry yeast powder weight fraction. Thermal conductivity declined from 3.76 W/m°C in specimen with 0% dry yeast powder weight fraction to 3.01 W/m°C in one with 25% dry yeast powder weight fraction. This thermal conductivity fall was caused by the increase in porosity. Porosity plays a critical role in the thermal conductivity decrease in solids because air or void has very low conductivity in comparison to solid matters.

The microstructures of the sintered specimens can be observed in Figure 10. The pores were nearly spherical in shape. According to Figure 10, porosity increased with the increase in the dry yeast powder weight fraction.

4. Conclusion

The research results indicate that with the increase in the content of dry yeast powder as a PFA (pore-forming agent) in the mixture with kaolin, the bulk density decreased (from 2.44 gr/cm^3 to 1.521 gr/cm^3), the porosity increased (from 23.77% to 52.48%), the compressive strength decreased (from 38.04 MPa to 4.51 MPa), and the thermal conductivity decreased (from 3.76 W/m^{o}C to 1.34 W/m^{o}C), each from 0% to 25% dry yeast powder contents. The raw material used was kaolin, which after being sintered at 1,450 °C transformed into mullite and cristobalite.

5. Acknowledgements

The authors would like to thank the Department of Mechanical and Industrial Engineering of the Faculty of Engineering, UGM, for providing research grant fund with contract no. 1576/H1.17/TMI/LK/2016.

6. References

Barsoum, M, 2003, Fundamentals of Ceramics, McGraw Hill, Singapore

Chen, C.Y. & Tuan, W.H., 2001, "The Processing of Kaolin Powder Compact", Ceramics Internationals (27), 795-800.

Chen, C.H., Takita, K., Ishiguro, S., Honda, S., Awaji, H., 2005, Fabrication of porous alumina tube by centrifugal molding, J. Eur. Ceram. Soc., 25(4), pp. 3257-3264.

Cristobalite data, http://webmineral.com/data/Cristobalite.shtml#.W9Ot1pMzY2w

Gregorova, E., Pabst, W, 2006, Porous ceramics prepared using poppy seed as pore-forming agent, Ceramics International.

Gregorova, E., Pabst, and Bohacenko, I, 2006, Characterization of different starch types for their application in ceramic processing, J. Eur. Ceram. Soc., 26 (8), pp.1301-1309.

Hammel E.C, Ighodaro, O.L.R, dan Okoli, O,I, 2014, Processing and properties of advanced porous ceramic: an application based review, Ceramics International, Vol 40(10), pp. 15351-15370

Kingon, A. I., & Davis, R.F., 2000, Engineering Properties of Multi-Component and Multiphase Oxides, in Ceramics and Glasses, Engineered Materials Handbook, Vol.4., ASM International, 758-774.

Lee, W.E. & Rainforth, W.M., 1994, Ceramic Microstructures Property Control by Prosessing, Chapman & Hall, Sheffield University.

Liu, P.S., dan Chen, G.F., Porous Materials, Processing and Applications, Tsinghwa University Press. 2014.

Manap, N.R.A, dan Jais, U.S., 2009, Influence of concentration of pore forming agent on porosity of SiO2 ceramic from rice husk, Material Research Innovations, Vol 13(3), pp.382-385.

Mullite data, http://webmineral.com/data/mullite.shtml#.W9Otc5MzY2w

Sandra, K., Budi, A., dan Susilo, A. (2014). Pengaruh Suhu Sintering Terhadap Densitas dan Porositas pada Membran Keramik Berpori Berbasis Zeolit, Tanah Lempung, Arang Batok Kelapa dan PVA. Jurnal Fisika, Fakultas Matematika dan Ilmu Pengetahuan Alam, Universitas Negeri Jakarta.

Wildan, MW, Suhanan dan Darwanto, 2009, Thermal conductivity and bending strength of porous mullite ceramics made by PFA method using corn starch, Jurnal Teknik Mesin ITS, Vol 9(3), hal. 149-155.

JOURNAL OF MATERIALS PROCESSING & CHARACTERIZATION

A Preliminary Study of 316L Stainless Steel Finishing Process by he Tumbling Method with Acrylic Abrasive Media

[1]F.P. Putera
[2]Suyitno

[1]Department of Mechanical and Industrial Engineering, Faculty of Engineering, Universitas Gadjah Mada. Jl. Grafika 2, Yogyakarta 55281, Indonesia

[2]Centre for Innovation of Medical Equipment and Devices (CIMEDs), Faculty of Engineering, Universitas Gadjah Mada, Yogyakarta 55281, Indonesia

Email: [1]finnyputera@gmail.com

Keywords
hip joint prosthesis, tumble finishing, surface roughness.

Abstract
A certain level of roughness of the surface of a hip prosthesis is necessary to minimize wear on components. Smoothing of the surface roughness can be performed by the tumble finishing method. This research was aimed to figure out the effect of spindle rotary speed on the level of roughness of the test specimen surface. The test specimen was made of 316 stainless steel, which is one of the materials constituting the component of the femoral head in a hip prosthesis. The abrasive media used was acrylic type plastic with a 4-mm-diameter spherical profile. The results of this tumbling process experiment demonstrate that the effective speed at which the cover surface of the test specimen was smoothed was the spindle rotary speed of 125 rpm.

Volume 1, Number 1, 2020, 9-13
DOI: http://dx.doi.org/10.22146/jmpc.v1i1.51408
e-ISSN: 2716-1285, ISSN: 2714-9722

1. Introduction

Degradation of hip joint function in medical terminology is referred to as hip osteoarthritis disease. In those suffering from osteoarthritis disease, the cartilage in the joint undergoes wear or thinning due to fraction (Cahyono, 2011). This wear or thinning will cause the surface of the hip joint cartilage corrugated and uneven. Aside from pain, hip osteoarthritis causes the hip joint to have disturbed motion, occasionally with noise, and even dislocation from the normal position (Cahyono, 2011).

Hip osteoarthritis can be overcome in a variety of ways, one of which is hip replacement with a hip prosthesis fitted into the body through surgical procedures. To create a good prosthetic hip joint, the component surfaces must be smooth so that the remaining contact stresses can be minimized (Chowdury et al., 2004). The smoothing process of the component surfaces in an artificial knee can be undertaken by deburring and finishing (Barletta et al., 2014).

Tumble finishing is suited for smoothing the femoral head component of hip joint prosthesis, which consists of internal and external surfaces. It is a high-efficiency, low-cost surface smoothing process of high efficiency with fine smoothing outcomes (Yang et al., 2017).

Tumble finishing involves rotation of a barrel containing abrasive media with a part immersed within, removing the coarse particles from machining on the internal and external surfaces of the part and leading to improved surface smoothness (Yang et al., 2017).

Figure 1 depicts the scheme for a tumble finishing process. In this process, the part and the abrasive media are placed in a barrel (container). When the barrel rotates at a predetermined speed, the part and the abrasive media will be lifted in the direction of the barrel rotation with influences from centrifugal, gravitational, and frictional forces. On the onset, the part and the abrasive media are positioned at the bottom of the barrel in an equilibrium, relatively motionless. When the part and the abrasive media are on the upper area of the barrel at a given height, the two objects will slide down. Then, the abrasive and part will tumble and initiate an abrasive process in the part.

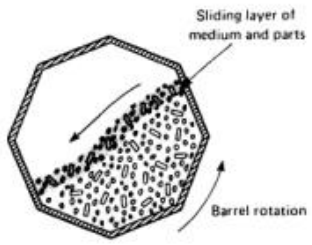

Figure 1. Tumbling scheme (Cotell et al., 1994)

A study pertaining to tumble finishing was carried out in a 2-mm-diameter spherical capsule in a 60-mm-long, 25-mm-diameter acrylic cylindrical container (Suratwala, 2012). The tumbling process lasted for 96 hours at a rotary speed of 100 rpm. The abrasive media used was glass with a silica colloid serving as a lubricant. It was concluded that this process successfully smoothened the surface of choice from an initial surface of 20 μm to 10 μm.

In the present study, the abrasive media used was plastic. A plastic abrasive media can produce a smooth surface faster than a ceramic one (Yang et al., 2017). A turning machine of which the rotating spindle is modified can be used as a tumbling machine. The quite high purchasing or fabricating cost for a tumble finishing machine led this research to using a turning machine with a modified rotating spindle. Althouh using a cheaper machine, we hoped that the surface roughness still can be decreased by using the tumble process. To reach it in this study, we examined an optimal paramaterto achieve the least rouhness when using the cheaper machine.

2. Methodology

Before tumble finishing is procesed, A barrel is manufactured. A barrel is a container where a test specimen is placed in a

turning machine. The barrel in this study was made of 201 SS in a cylindrical form with covering 6 mm thick. The container was 164 mm in external diameter and 160 mm in height. The size was adjusted to the space within the turning machi ne. The design of the barrel must meet the wear-resistance criteria as the wall of the barrel would often rub on the test specimen and the abrasive media.

The abrasive media used in this tumble finishing process was an acrylic type plastic media. The acrylic used had a spherical profile 6mm in diameter. A plastic abrasive media is reliable during deburring, ball burnishing, drying, and dry polishing processes (Holzknecht, 2009). The abrasive media used was then placed into a 36-cm-diameter stainless steel barrel (201 SS). The amount of the abrasive media was 5 kg. The abrasive media used in this tumble finishing was 6 mm deep acrylic type plastic. This acrylic type was available in jewelry-accessory stores because its initial designation is for jewelry beads. Standard abrasive media for finishing applications was not readily available in Indonesia.

The specimen used was a solid cylindrical specimen with a hole giving it an internal surface, shaped like a femoral head. This specimen was made of a 316L stainless steel material. The dimensions were 16 mm in diameter and 25 mm in length. These material selection and geometrical determination were performed according to the material and the geometrical shape of the hip prosthesis femoral head as shown in Figure 2.

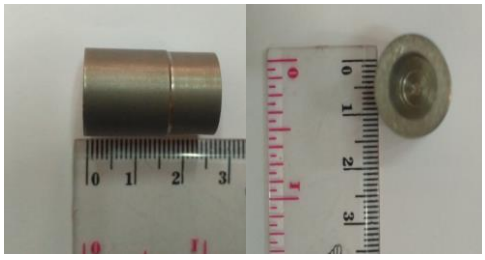

Figure 2. Specimen

Prior to the start of the tumble finishing in the femoral head component, tumble finishing was first performed on the specimen to minimize the frequency of femoral head component use in this research out of high cost of femoral head component.

The test specimen shown in Figure 2 was manufactured through processes from cutting, to drilling, to surface lathing until the desired size was achieved. Then, surface lathing was performed to feed the specimen surface to obtain uniformity in the initial surface roughness measure of the specimen. This process was conducted using a CNC lathe machine with feeding 0.4 mm deep, resulting in 0.704 μmRa of mean initial surface roughness of covering.

After the barrel, abrasive media and test specimen were made available, the tumble finishing was started. The tumble finishing process is carried out at various spindle speeds (40, 85, 125 and 180 rpm) with the same number of turns of 2400 turns.

During the tumbling process, the barrel was rotated by the turning machine spindle, causing the abrasive media along with the part within the barrel to rotate. The speed that results in the lowest surface roughness change then used to test the effect of finishing duration on roughness surface. The duration used varies (10, 20, 30, 60 minutes) until there is no change in Ra> 0.01 μm. In each variation the surface roughness of the test specimens is measured.

The measurement of the initial and final surface roughness of the test specimen produced from surface lathing was performed using the stylus profilometer surface roughness measuring instrument. Part of specimen measured as shown ini Figure 3. The surface roughness is measured three times on different specimens.

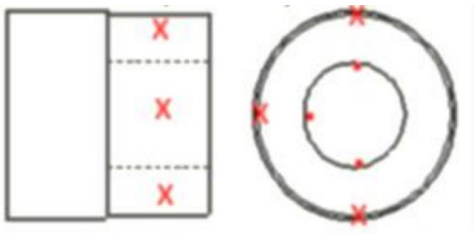

Figure 3. Part of specimen measured

3. Results

The outcomes of the tumble finishing process with the spindle rotary speed made variable with surface roughness can be seen in Figure 4. The value of surface roughness was measured with mean (filled circle) and standard error (errorbar).

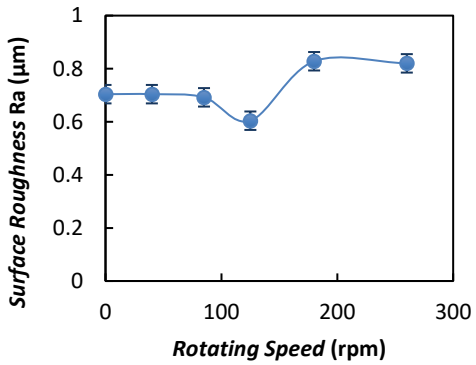

Figure 4. Chart of the effect of rotary speed (rpm) on surface roughness

Based on the chart in Figure 3, the lowest roughness value obtained was 0.604 µmRa. At first, the surface roughness values barely changed from 40 rpm to 85 rpm speeds, but a decline was observed at 125 rpm. This means that at 125 rpm, the finishing process was running effectively in the tumbling because the increased rotation speed was followed with increased centrifugal force, causing the finishing process to start in the barrel (Yang, 2006). When the rotary speed increased, the part and the abrasive media would also rotate (roll) faster and slide down more often.

However, the surface roughness increased even further at 180 and 260 rpm. This was estimated to happen because the tumbling process had passed the effective maximum speed, so the part and the abrasive would cling to the barrel wall during the tumbling process.

After getting the best speed at 125 rpm, then followed by the tumbling process using that speed with vary the duration. The value of surface roughness can be seen in Figure 5. The value of surface roughness was measured with mean (filled circle) and standard error (errorbar).

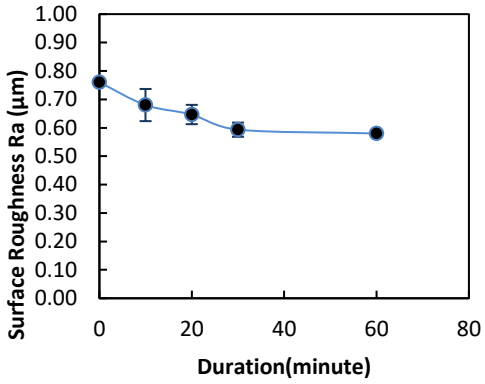

Figure 5. Chart of the effect of duration (minute) on surface roughness

The Figure 4 shows that an increase in finishing duration will causes a decrease in surface roughness to the point of saturation where an increase in duration no longer causes a decrease in roughness significant. Significant decrease in surface roughness still occurs when the duration is 30 minutes which results in surface roughness of 0.59 µm. After increasing the duration by more than 30 minutes, the decrease in surface roughness did not occur significantly.

4. Conclusion

Finishing process in 316L SS as a hip prosthesis material can be performed through a tumble finishing process with a 6-mm-diameter spherical acrylic abrasive media. This tumble finishing used a turning machine to rotate a barrel containing an abrasive media and a test specimen. From the finishing processes conducted, it was found that the effective maximum rotary speed at which the lowest surface roughness was obtained was 125 rpm.

5. References

Barletta, M., Pietrobono, F., Rubino, G., Tagliaferri, V., 2014, Drag finishing of sensitive parts with fluidized abrasives, Journal of Manufacturing Processes, Volume 16, pages 494-502.

Cahyono, I., 2011, Simulasi Kontak Komponen Acetabular pada Sambungan Tulang Pinggul Buatan Menggunakan Metode Elemen Hingga, Universitas Dipenogoro.

Cotell, C.M., Sprague, J.A., Smidt, F.A, 1994, Surface Engineering,ASM Handbook, Volume 5

Chowdury, S.K.R., Mishra, A., Pradhan, B., dan Saha, D., 2004, Wear Characteristic and biocompattibility of some polymer composite acetabular cups, Wear, Volume 256, Pages 1026-1036

Holzknecht, E., 2009, Everything you need to know about mechanical/mass finishing: a workshop on the role of media in mechanical surface finishing, Metal Finishing, Volume 107, Pages 27-31.

Suratwala, W.A., Steele, M.D., Feit, K., Moreno, M., Stadermann, J., Fair, K., Chen, A., Nikroo,K., Youngblood, K., 2012, Polishing and local planarization of plastic spherical capsules using tumble finishing, Applied Surface Science 261 Pages 679–689

Yang, S., Li, S.W., 2017, Surface finishing theory and new technology, 1st ed., Springer, Beijing.

JOURNAL OF MATERIALS PROCESSING & CHARACTERIZATION

Tensile Strength of Carbon Fiber/Epoxy Composite Manufactured by the Bladder Compression Molding Method at Variable Pressure Levels

[1]I. H. Ismadi
[2]G. Nugroho

[1,2]Department of Mechanical and Industrial Engineering, Faculty of Engineering, Universitas Gadjah Mada. Jl. Grafika 2, Yogyakarta 55281, Indonesia

[1]Manufacturing Engineering, Politeknik ATMI Surakarta, Jl. Adisucipto/Jl. Mojo no. 1, Karangasem, Laweyan, Surakarta, 57145, Tlp. 0271 714466

Email: [1]henry.ismadi@atmi.ac.id

Keywords
bladder compression moulding, epoxy, vacuum bagging.

Abstract
Composite materials uses have been increasingly ubiquitous due to their advantages, for example, in being strong, lightweight, and rust-resistant. Various composite manufacturing processes are designed to obtain composite products of better quality, including minimizing the number of pores or voids trapped within and increasing the fiber volume fraction until an optimal value is achieved. The method employed in this research was the bladder compression molding method, and the materials used were woven carbon fabric and epoxy matrix. According to previous research which used this method, the higher the pressure in the bladder, the better the product quality generated. The aim of this research was to investigate the effect of changes in the pressure level in the bladder (1, 2, 3, 4, 5, 6, 7, and 8 bar) on the mechanical properties of the composite produced. The test specimen was gained by cutting the composite product with a CNC router machine. The tensile test results indicate that the ultimate testing tensile strength was 604 MPa and that the optimal pressure in the bladder was 7 KPa. The conclusion of this research is that the composite product quality would increase with the progressive increase in the bladder pressure to the point of optimal pressure.

Volume 1, Number 1, 2020, 15-21
DOI: http://dx.doi.org/10.22146/jmpc.v1i1.51411
e-ISSN: 2716-1285, ISSN: 2714-9722

1. Introduction

Currently, uses of composite materials as alternatives to metal components in various equipment are omnipresent. This is inextricably linked to a number of important advantages of composite products over other preceding components. Composites' properties of being corrosion-resistant and strong but lightweight make them easy to be accepted as substituting components which increase their reinforced products' physical values (Callister Jr. and Rethwisch, 2014).

In general, composite fabrication is performed by combining reinforcing fiber and matrix. The constituents are applied one after another or as a mixture to the surfaces of a mold (Partridge, 2016). The requirement of a quality mold that ensures uniformity of the product's shape for repeated production processes puts composite fabrication into a relatively expensive category. Some prevailing composite fabrication processes are the result of constant upgrading carried out to obtain high-quality composite products and to achieve an increased efficiency to minimize the production cost. Each fabrication process has distinct advantages and disadvantages, both in terms of product quality (shape, surface quality, and mechanical properties) and in terms of process effectiveness and efficiency (process cycle time, energy need, and the impacts such fabrication process exerts on the environment).

The simplest composite fabrication processes generate products with relatively low fiber and resin density or relatively small fiber and matrix volume fractions (Partridge, 2016), for example, those using the hand lay-up and spray-up methods. The subsequent fabrication processes are developed in such a way that the composite products yielded have better quality. As such, the complexity of the processes and, at the same time, the costs for production also increase. Examples of such sophisticated methods include the vacuum bagging and autoclave methods.

It is also essential to pay attention to the bonding or joining of two composite-composed components. Often time, it is at this point that a construction design which involves composite materials is weak. Manufacturing of capsule-shaped objects for maritime and aviation purposes, for example, is often performed simply by joining two mold component pieces by gluing or riveting, while the water or air pressure such components receive is quite high. Risk of damage or leakage at the joint may lead to fatal consequences for the entire construction. The bladder molding composite fabrication method was developed for overcoming such problem, especially in meeting the need for composite products in jointless cylindrical shapes. Hi-tech products in the aviation field like unmanned aircrafts will find this method extremely helpful for their development. The bladder or balloon, which serves as the core of the mold, will be wrapped in the reinforcing fiber material along with the resin, then placed between two mold parts for the outer part formation. During the curing process, pressure is applied into the bladder to give better compactness to the composite product (Anderson and Altan, 2014). However, it has been hard to gain information regarding the ideal pressure needed to obtain a composite product with maximum density although such information will be very helpful for the composite fabrication process for specific purposes in the days to come.

This research, which employed the bladder molding method, was aimed to gain the optimum pressure value for the bladder and the ultimate strength of the composite products processed under this pressure.

2. Methodology

This research used twill weave carbon fiber fabric with weight per area of 240 g/m2 as the reinforcing fiber and bisphenol A-epichlorohydrin type epoxy resin mixed with cycloalipathic anine type EPH 55 epoxy hardener at 1:1 ratio as the matrix. A composite specimen was manufactured with the bladder molding method, aided with the hand lay-up method for the initial application of fiber and resin upon a pair of closed mold

parts made from series 6 aluminum as shown in Figure 1.

Figure 1. Aluminum mold

Meanwhile, the bladder was manufactured from silicone rubber with RTV-blue catalyst as a hardening agent using the same mold before it is used for molding the composite.

All of the raw materials along with the technical data as listed in Table 1 (Li et al., 2015) were provided by the Mechanical Technology Laboratory, Department of Mechanical and Industrial Department, Universitas Gadjah Mada Yogyakarta, while the research was conducted at the Central Plastics Technology Laboratory, Politeknik ATMI Surakarta, using central compressor Ingersoll Rand type XK06-010-00512 at maximum pressure of 1 MPa.

Table 1. Fiber and matrix technical data

Technical data	Fiber	Matrix
Density [g/cm^3]	1.8	1.18
Tensile modulus [GPa]	18	3
Tensile stress [MPa]	4,900	67

The bladder was manufactured by mixing silicone rubber and the catalyst in a container at a weight ratio of 50:1, stirring the mixture well, then pouring it into the hole of each mold part. Over each pool was placed a piece of Styrofoam with a weight applied. Hence, after the curing process was complete, holey silicone rubber pieces were obtained (Figure 2).

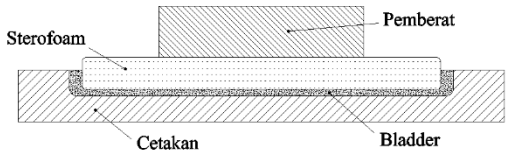

Figure 2. Bladder manufacturing

The two bladder pieces were then glued together with a binder of the same material with an air tube previously fitted (Figure 3).

Figure 3. Bladder

The next step was preparing the fiber and matrix. The woven carbon was cut 170 x 325 mm2 in size, while the epoxy resin was mixed with the hardening solution in a container. The two mold parts were prepared near each other, then the cavities were smeared with wax for easy removal of the composite produced. Woven carbon was used for easy placement on the mold parts, especially for mold contour with an intricate shape (Hancock and Potter, 2006).

Resin was applied on the surface of the two mold parts over which wax was smeared, than one piece of woven carbon sheet was laid on each part. Resin was applied over the woven carbon sheet, and the next sheet was laid. This went on until there were six fiber layers on each mold cavity surface before finally concluded with resin smear. On the topmost layer was placed a perforated sheet of plastic (breather) which would let the excess resin flow from the composite arrangement. Then, a piece of white flannel fabric as the excess resin absorber was laid as a covering layer. The bladder was placed on the layers on the lower mold part, and the lower and upper mold parts, along with all of the filling layers, were closed together, causing

the bladder to be sandwiched. The two mold parts were held together in place with 6 M12 imbush bolts. After the mold was clossed with bolts fastened, the air tube from the central compressor was connected to the air tube that run toward the bladder through a regulator as shown in the experimental setup in Figure 4.

Figure 4. Experimental setup

The air pressure from the XK06-010-00512 type Ingersoll Rand central compressor (Figure 5) was adjusted by the regulator, starting from p = 100 KPa. The process lasted for approximately 22 hours until the epoxy curing at room temperature was complete. The composite product was removed from the mold (Figure 6), which would be used for process repeats at different levels of pressure according to the data in Table 2.

Table 2. Variable pressures

Process Pressure		Process Pressure	
1	100 MPa	5	500 MPa
2	200 MPa	6	6`00 MPa
3	300 MPa	7	700 MPa
4	400 MPa	8	800 MPa

Figure 5. Central compressor

Figure 6. Composite produced

The composites produced were removed from the bladder and mold, then cut with an end mill cutter 4 mm in dimension for tensile testing using a CNC Router machine. From each composite piece produced at different bladder pressure, five tensile specimens were taken according to ASTM D638 in shape and dimension as shown in Figure 7.

Figure 7. Tensile Test Specimen

The specimens were tested using Universal Testing Machine Zwick Roell type N020 with maximum tensile strength of 20 kN (Figure 8) after measurement of the fracture section of each specimen using a 0.01-mm-accuracy 0–25 mm Mitutoyo outside micrometer.

The maximum stress values of the five tensile test specimens for each process were averaged and then compared with each other so that the optimum pressure value for the woven carbon fiber/epoxy resin composite manufacturing process by the bladder molding method as well as the maximum tensile strength of the product could be obtained.

Figure 8. Tensile test process

3. Results and Discussion

The tensile test results, including the maximum force required, tensile strength until point of fracture, tensile modulus, and fracture stress, are outlined in Table 3.

Table 3. Tensile test results

No.	Pressure [KPa]	Force [N]	σ_M [MPa]	E_T [GPa]	ε [%]	Thickness [mm]	Width [mm]	Area [mm^2]
1	100	12,078.49	435.457	51.422	0.89	2.26	12.25	27.74
2	200	11,298.39	500.027	47.691	1.05	1.81	12.53	22.65
3	300	13,190.27	500.144	41.756	1.20	2.12	12.49	26.46
4	400	11,892.40	510.582	41.226	1.24	1.86	12.50	23.29
5	500	10,950.81	493.169	41.153	1.20	1.77	12.59	22.24
6	600	10,748.90	457.273	41.652	1.10	1.86	12.63	23.55
7	700	12,816.77	604.948	56.290	1.08	1.69	12.53	21.20
8	800	11,550.51	520.817	44.172	1.18	1.78	12.51	22.29

Table 3 shows that the higher the pressure was exerted to the bladder, the lower the thickness of the composite products (Anderson, et al., 2013). The trend line logarithmically presented in Figure 9 provides an illustration for that trend. The flannel fabric placed between the perforated plastic (breather) and the bladder functioned well. The bladder's pressure forced the excess resin out from between the woven carbon fabric layers through the small holes of the breather. The excess resin was absorbed well by the flannel fabric. Thus, after the completion of the process, the bladder looked as though wrapped in a film. This film was the resin-absorbing flannel fabric which indirectly protected the bladder against the sharp edges of the tools used to remove the composite product from the mold cavities. Besides, the ring set between the mold parts when closed kept a space between the mold surfaces, giving a room for the excess resin unabsorbed by the flannel fabric to flow. The excess resin that was unabsorbed by the flannel fabric dried

during the curing process on the mold surfaces, making it easy for removal.

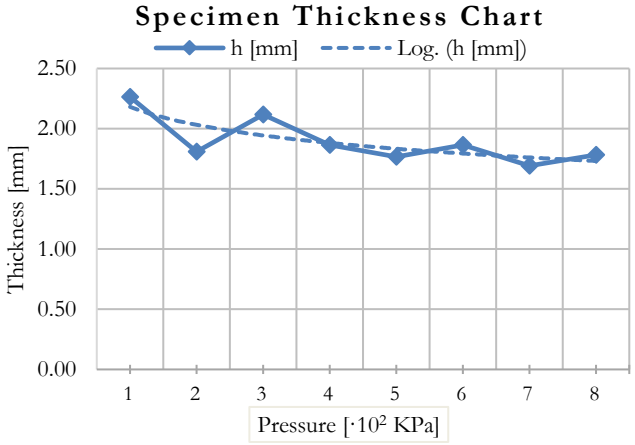

Figure 9. Specimen thickness chart

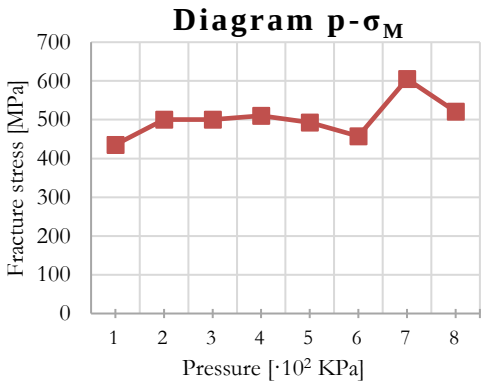

Figure 10. Pressure-fracture stress chart

Figure 11. Difference in stiffness and thickness between pieces of woven carbon fabric

The values of fracture stress compared to the bladder pressure during the tensile test in respective units (pressure in KPa, fracture stress in MPa) are shown in Figure 10. It can be observed that the specimens' fracture stress values would increase if the bladder pressure levels also increased. Thus, the maximum fracture stress value of 604.948 MPa was reached at bladder pressure of 700 KPa. The fracture stress values at bladder pressure levels 500 KPa, 600 KPa, and 800 KPa were outside the expectation area. This was presumably caused by the difference in thickness and stiffness of the woven carbon fiber materials used in this research, which was accepted in several deliveries, as shown in Figure 11. Another possible cause was that the area of the flannel fabric prepared for absorbing the excess resin differed from process to process and from process level to another.

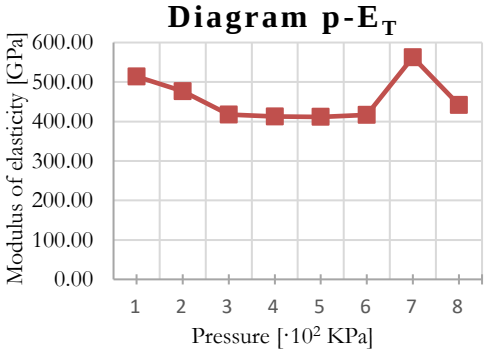

Figure 12. Pressure-tensile modulus chart

The same was the case in the tensile modulus. As can be observed in Figure 12, the tensile modulus values (in MPa) were compared to the bladder pressure levels (in KPa). At bladder pressure 70 KPa, the tensile modulus reached the highest value, namely 562.9·102 MPa. This value is higher than when the bladder pressure was at 800 KPa. In this case, the difference in the stiffness of the raw materials, especially woven carbon fiber, tended to have a significant effect (Gibson, 2012).

4. Conclusion

From this research, a number of conclusions were drawn:

1. The maximum fracture stress value of the composite material produced using the bladder compression molding was 604.948 MPa, which was reached at bladder pressure 700 KPa.
2. The maximum tensile fracture value of the composite material produced using the same method was 56.29 GPa, also at bladder pressure 700 KPa.
3. The composite material produced would tend to be thinner when the bladder pressure also increased, with the potential of decreased resin content or increased fiber volume fraction in the composite.
4. A further study with bending and density tests on the composite manufactured by this method is deemed necessary to gain more detailed information regarding the mechanical properties of the composite.

5. References

Anderson, J. P., & Altan, M. C. (2014). Bladder Assisted Composite Manufacturing (BACM): Challenges and Opportunities. Research Gate.

Anderson, J. P., Kelly, A. J., & Altan, M. C. (2013). Fabrication of Composite Laminates by Vacuum-Assisted Resin Transfer Molding Augmented with an Inflatable Bladder. Research Gate.

Callister Jr., W. D., & Rethwisch, D. G. (2014). Materials Science and Engineering. Danvers, MA 01923: John Willey & Sohn, Inc.

Gibson, R. F. (2012). Principles of Composite Material Mechanics. Boca Raton, FL 33487-2742: CRC Press Taylor & Francis Group.

Hancock, S. G., & Potter, K. D. (2006). The use of kinematic drape modelling to inform the hand lay-up of complex composite components using woven reinforcements. Composites Part A 37 : Applied Science and Manufacturing, 412-422.

Li, Y., Li, R., Lu, L., & Huang, X. (2015). Experimental study of damage characteristics of carbon woven fabric/epoxy laminates subjected to lightning strike. Composites: Part A 79 (2015), 164-175.

Partridge, I. (2016). NetComposites. Retrieved from NetComposites Web site: https://netcomposites.com/guide-tools/guide/manufacturing/cure-monitoring/

JOURNAL OF MATERIALS PROCESSING & CHARACTERIZATION

Tensile Strength of Carbon Fiber/Epoxy Composite Manufactured by the Bladder Compression Molding Method at Variable Curing Temperatures

[1]A. D. Setyoko
[2]G. Nugroho

[1]Master's Degree in Mechanical Engineering, Department of Mechanical and Industrial Engineering, Universitas Gadjah Mada Jl. Grafika 2, Yogyakarta 55281, Indonesia

[2]Manufacturing Engineering, Politeknik ATMI Surakarta, Jl. Adisucipto/Jl. Mojo no. 1, Karangasem, Laweyan, Surakarta, 57145, Tlp. 0271 714466

Email: [1]dwi.setyoko@atmi.ac.id

Keywords
bladder compression molding, mechanical property, carbon fiber-epoxy composite.

Abstract
Corrosion-resistant, high-strength, low-density composite materials are seeing increased applications in a wide variety of products. The composite constituents of matrix and reinforcement require molding technologies and methods to generate products. The bladder compression molding method is an effective method of manufacturing of composite products with a tubular shape, cavity, and/or closed contour. The properties of the composite materials produced are determined by three variables, namely curing pressure, temperature, and time. This research was conducted to learn the effect of temperature on the mechanical properties of the composite materials produced from the process with the bladder compression molding method. Based on the thickness, tensile strength, and modulus of elasticity of the product from the experiment conducted, the optimal temperature of the process was found to be 120 °C.

Volume 1, Number 1, 2020, 23-30
DOI: http://dx.doi.org/10.22146/jmpc.v1i1.51413
e-ISSN: 2716-1285, ISSN: 2714-9722

1. Introduction

Use and utilization of composite materials have recently been increasingly widespread and developing. Composite materials start to find applications as product components in place of other materials. This increasingly prevalent composite use is due to the advantages the composite carries, including corrosion resistance, strength, and low density (Anderson & Altan, 2014). The growing use and utilization of these composite materials also have an impact on the development of manufacturing technologies in the making of products from composites.

A composite is a mixture of two separate materials or more that can be composed of metal, ceramic, and polymer materials. A composite is able to bring up the properties not expressed by the individual constituents and at the same time join together the best properties of each of the materials (Callister & Rethwisch, 2014). A composite is made up by matrix and reinforcement. The basic constituents of the composite come with distinct basic properties which are combined to produce a single material with better properties. The bringing up of the superior properties desired is highly dependent on the technologies applied in the composite manufacturing process. One of the technologies that can be applied in a manufacturing process is the bladder compression molding.

The bladder compression molding is an effective method of composite manufacturing as it has the capability of forming the outer surface through a negative mold and the inner surface with application of bladder (balloon) pressure. This specific method is highly useful for production of items with a tubular, hollowed, or other closed-contour form (Anderson and Altan, 2012). Using mold, this method comes as extremely handy in the mass production of small- to medium-sized components of complex geometries (Anderson, 2014). The use of a mold also minimizes secondary cutting operations. In the bladder compression molding method, the combining of the materials is performed using top and bottom parts of a mold and a bladder (balloon). The upper and lower mold parts have the negative form of the product, while the bladder the positive, following the shape of the product to be manufactured. The bladder functions as a suppressor of the materials to be mixed. With this application of pressure, the constituents can properly be combined together and shaped after the mold over a curing process. Other than pressuring, heating at a given temperature and over a given period is also performed during the curing process. The properties of the composite materials produced are highly dependent on the three variables above: the pressure, temperature, and time applied during the curing process.

To obtain optimal mechanical properties and characteristics from an epoxy composite, the composite must be subjected to a curing cycle from which epoxy density with a high cross-link level is generated (Gibson, 2012). This curing cycle involves a combination of curing temperature and time. Higher curing temperatures produce more refined reactions with higher cross-linking levels than do lower temperatures. For optimal cross-linking density, a curing process at a fairly high temperature will produce sufficient kinetic energy for a more even chemical reaction. Generation of a high cross-linking density will enable the composite previously subjected to a curing process to exhibit the best mechanical and physical properties. On the other hand, the application of a sub-optimal curing temperature will cause the epoxy to undergo an excessively fast curing process. This excessively fast curing process will lead to the formation of residual stress which will harm the mechanical properties and characteristics of the composite produced. Curing temperatures that reach the glass-transition temperature (Tg) will subject the composites to degradation of properties related to stiffness, heat capacity, and thermal expansion (Callister & Rethwisch, 2014). Thus, all composite formation methods, including bladder

compression molding method, require a close attention in the determination of the curing parameters, especially temperature.

The objectives of this research were 1) to develop a system and equipment of composite manufacturing by the bladder compression molding method, 2) to analyze the effect of curing temperature on tensile strength in composites of epoxy matrix and reinforcing carbon fabric manufactured by the bladder compression molding method, 3) to analyze the effect of curing temperature through tensile testing in composites of epoxy matrix and reinforcing carbon fabric manufactured by the bladder compression molding method, and 4) to obtain data of optimal curing temperature in the manufacturing of composites of epoxy matrix and reinforcing carbon fabric by the bladder compression molding method.

2. Methodology

This research stressed the composite formation process with the bladder compression molding method.

This method was applied with a mold that had a rectangular mold hollow 235 mm long, 180 mm wide, and 20 mm thick. Every corner of the lengths and widths of the mold hollow had a 10-mm radius and the corner of the thickness a 6-mm radius. The mold had two parts: the upper and the lower ones. Every mold part was equipped with a heater and a thermo control used for adjusting the curing temperature.

To obtain the composite form and density of interest, a bladder was used as a mold core. The bladder was made from silicon rubber approximately 5 mm thick. A piece of sheet was shaped following the shape of the mold hollow on the lower mold part. Each part had a mold cavity and heating cavity on the rear side. The heating cavity was smaller in size.

In this research, the pressure of the bladder was maintained at 5 bar over the composite resin curing process.

The process stages involved in this research can be described in the chart in Figure 1.

Mold manufacturing started from the designing, material ordering, and machining. The mold manufactured consisted two upper parts and covers. The mold used for making the composite specimen in this research was made from aluminum. The dimensions of the mold on the outside were 322 mm in length, 240 mm in width, and 40 mm in thickness. Meanwhile, the cavity of the mold was 262 mm long, 180 mm wide, and 20 mm thick. The sketch of the mold dimensions can be seen in Figure 2.

The bladder was made from silicon rubber. Silicon rubber was cast into a bladder in the mold. As with the mold for forming the specimen, the bladder mold also consisted of two main parts: upper part and lower part, each of which also came with a cavity.

Bladder forming was performed in the following steps: 1) prepare the mold (upper and lower) in an open state, 2) smear oil or release gel on the surface of the cavity thinly and evenly, 3) apply silicon rubber or latex rubber on the cavity of both mold parts and wait for some time, 4) close the two mold parts together after the silicon rubber or latex rubber was considered to start thickening but was still glueable, and 5) after the material was estimated to have hardened, the mold was opened and the bladder was removed from the cavity.

After the mold, bladder, heater, and control system were assembled, composite forming with the bladder compression molding method could be performed.

The composite product was formed by first applying release gel on the mold, then applying reinforcing fiber and resin alternately to form composite layers, placing a bladder between the upper and lower mold parts and then closing them together, applying pressure on the bladder, and adjusting the heat through the thermo control.

After 90 minutes, the composite product forming process was ended.

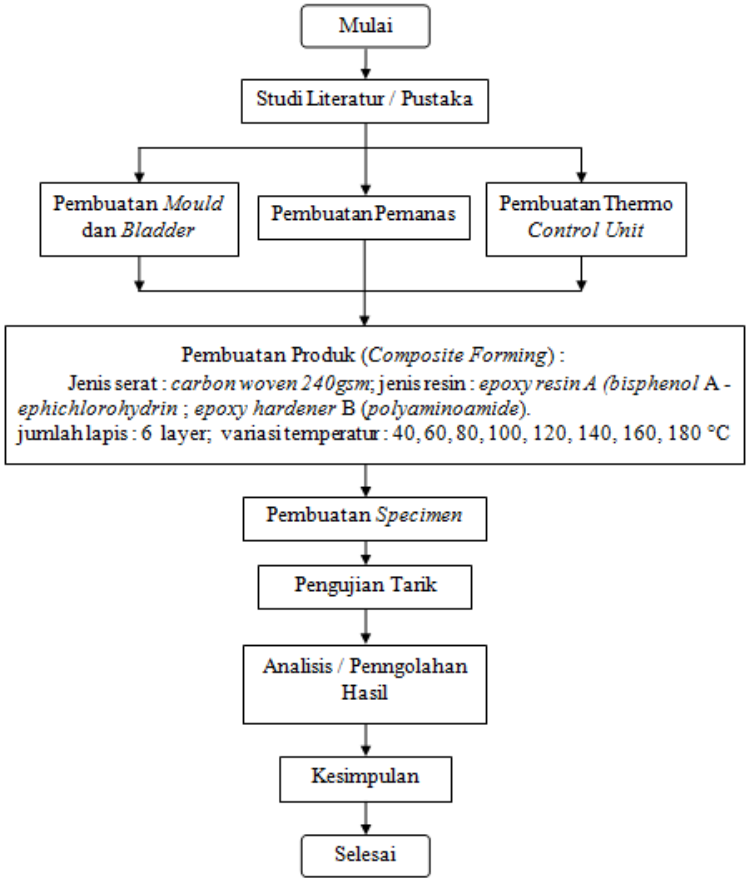

Figure 1. Research Flow Chart

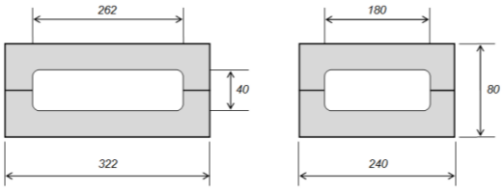

Figure 2. Composite Mold Dimensions

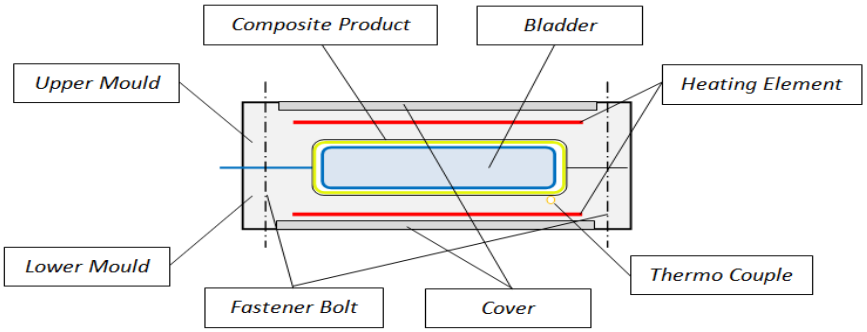

Figure 3. Bladder Compression Molding Unit Sketch

The equipment used for the composite product forming consisted of 1) a mold set equipped with a heater and a thermo control, 2) a temperature control unit, 3) a bladder core with nipple compressor, 4) regulator valve, and 5) pneumatic hose.

Meanwhile, the materials used were 1) reinforcement from 240 gsm of carbon clothe woven (fabrics) and 2) a matrix from epoxy resin A (bisphenol A-epichlorohydrin) and epoxy harderner B (polyaminoamide).

Figure 4. Composite Materials

The materials used in forming the composite product with the bladder compression molding method are shown in Figure 4.

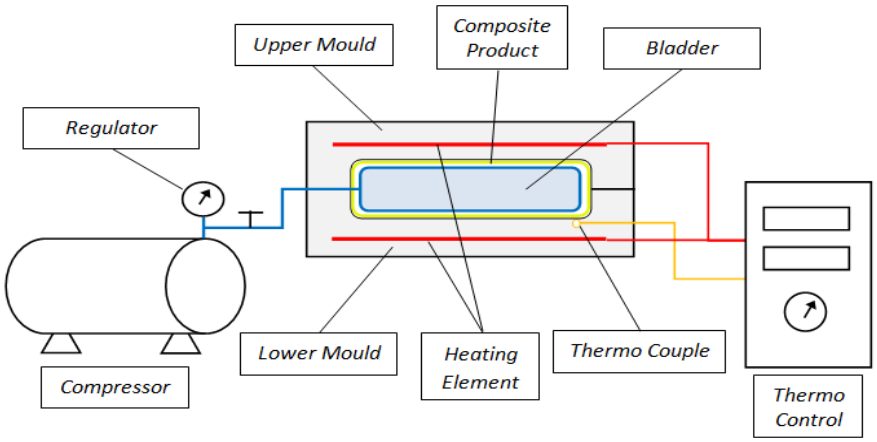

Figure 5. Composite Formation with the Bladder Compression Molding Method

The scheme of the composite formation process with the bladder compression molding method is shown in Figure 5, and the implementation in Figure 6.

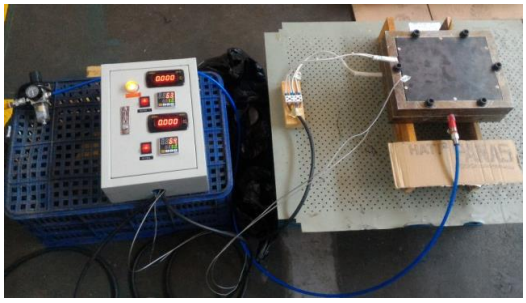

Figure 6. Implementation of Composite Forming with the Bladder Compression Molding Method

The steps of the composite making can be outlined as follows: 1) smear release gel on the cavity surface thinly and evenly; 2) apply fiber and n on the mold and bladder in six layers; 3) place all of the materials prepared previously into the bladder mold, then close the mold with bolts fastened; 4) inflate the bladder until a pressure of 5 bar is reached; 5) heat the heater until the mold reaches a curing temperature and keep the temperature for 90 minutes; 6) cease the heating and start cooling; and 7) lower the bladder pressure until zero and remove the specimen from the mold.

The composite produced from this process with the bladder compression molding method was then tested for its mechanical properties. This test was useful to figure out the quality of the product.

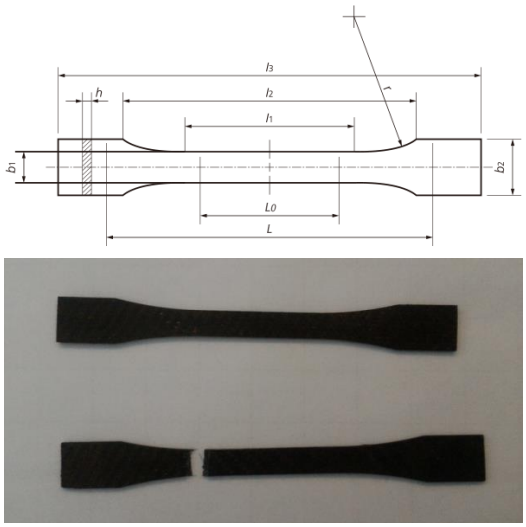

Figure 7. ASTM D638 Tensile Test Object

The mechanical properties were identified through a tensile test. Thus, this product was then cut using a router machine in a shape meeting the ASTM D638 tensile test standard with the observed part being b1 = 12.4 mm in width and Lo = 50 mm in length (ASM Handbook, 2000). The tensile test object and the testing process are shown in Figures 7 and 8.

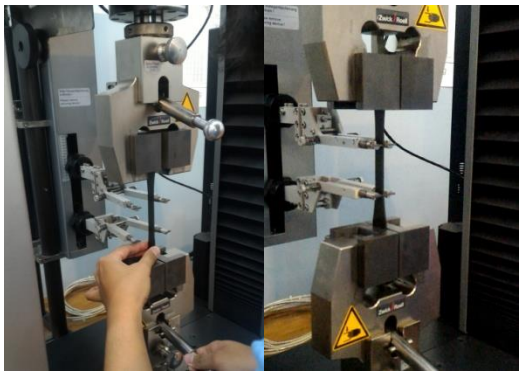

Figure 8. Fixing and tensile testing of the composite product with the ASTM D638 method in the test machine

3. Results and Discussion

From the observation conducted during the product manufacturing process with the bladder compression molding method, it was found that temperature affected the curing process speed and the liquidity of resin before the curing process. The speed and the amount of cross-linking affected the bond structure formed in the resin and the carbon fiber as reinforcement. This impact can be seen in the product strength as obtained from the tensile testing.

From the tensile testing, some data were obtained as presented in Table 1. The data demonstrate how temperature affected the dimensions and the properties of the composite product manufactured with the bladder compression molding method.

The effect of curing temperature on the product geometries can be observed from the product thickness resulted (Figure 9).

The test object thickness tended to decrease when the temperature was increased from 40 °C, and a minimum thickness was reached when the temperature was at 120 °C. Past 120 °C, the object tended to increase in thickness. The product thickness for each process temperature parameter is shown in Figure 9.

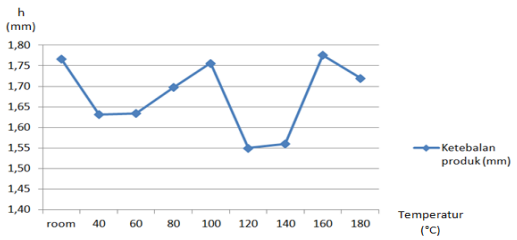

Figure 9. Chart of the Relationship between Product Thickness (h) and Curing Temperature

Table 1. Tensile Test Result Data

No	Temp	Force	Et	σM	σB	h	b	A_0
	°C	N	MPa	MPa	MPa	mm	mm	mm^2
1	room	10950,81	41060	493	493	1,77	12,59	22,24
2	40	11301,85	48900	557	557	1,63	12,46	20,33
3	60	9357,46	41780	465	465	1,63	12,35	20,17
4	80	9562,92	40600	453	453	1,70	12,49	21,20
5	100	10124,33	39340	455	455	1,76	12,67	22,24
6	120	11510,94	49920	591	591	1,55	12,56	19,47
7	140	10632,98	43800	544	544	1,56	12,56	19,60
8	160	10978,92	41280	499	499	1,78	12,52	22,21
9	180	11215,76	49560	523	523	1,72	12,47	21,45

The test object thickness tended to decrease when the temperature was increased from 40 °C, and a minimum thickness was reached when the temperature was at 120 °C. Past 120 °C, the object tended to increase in thickness. This was attributed to the change in the liquidity at every process temperature and the resin hardening speed over the curing process. At constant pressure of 5 bar, more liquid resin would flow absorbed into the reinforcing fiber. It was also easier for the excess resin volume to break out from the product and mold through the breather and gaps at the mold periphery. The product's thickness rebounded at 160 °C because curing processes speed up at high temperatures.

The effect of curing temperature on the product's tensile strength is shown in Figure 10. This figure shows that tensile strength was inclined to drop at temperatures between 60 °C and 80 °C then bounce back at 100 °C to 120 °C. At temperatures 140 °C and 160 °C, the tensile strength fell again.

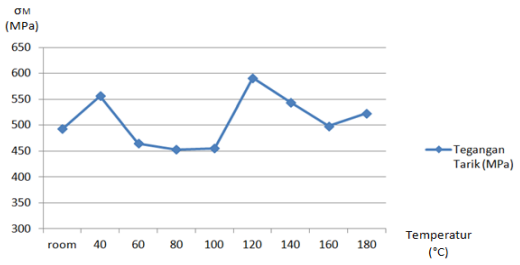

Figure 10. Chart of the Relationship between Tensile Strength (σM) and Curing Temperature

The increase in the product's tensile strength was resulted from the strengthening bond between resin and fiber where resin became more liquid at high temperatures and from the product's thinner dimension. With the same fiber volume and thinner product dimension, it can be concluded that the fiber's volume fraction was higher.

Figure 11 shows the effect of curing temperature on the modulus of elasticity of the product that was manufactured with the bladder compression molding method. The trend was identical with that of the tensile strength changes.

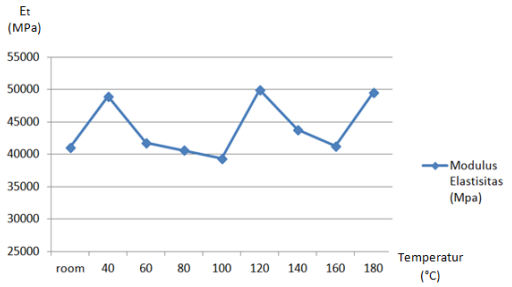

Figure 11. Chart of the Relationship between Modulus of Elasticity of the Product and Curing Temperature

4. Conclusion

In the composite manufacturing with the bladder compression molding method, temperature played a pivotal role influencing the product's quality.

1. Temperature had effects on the product's thickness, tensile strength, and modulus of elasticity.
2. The composite produced by the bladder compression molding had the lowest thickness at the curing temperature 120 °C.
3. The tensile strength and modulus of elasticity of the composite produced by the bladder compression molding reached a maximum at the temperature 120 °C
4. From the data outlining and analysis, it is concluded that the optimal curing temperature for the composite forming by the bladder compression molding is 120 °C.

5. References

Anderson, J., & Altan, M. (2012). Properties of Composite Cylinders Fabricated by Bladder Assisted Composite Manufacturing . Journal of Engineering Materials and Technology 134, 1-7.

Anderson, J., & Altan, M. C. (2014). Bladder Assisted Composite Manufacturing (BACM): Challenges and Opportunities. Polymer Processing Society Europe-Africa Conference (hal. DOI10.13140/2.1.2139.6169). Tel Aviv: ResearchGate.

Anderson, J., Kelly, A., & Altan, M. (2013). Fabrication of Composite Laminates by VacuumAssisted Resin Transfer Molding Augmented with an Inflatable Bladder. Researchgate, 2-13.

Askeland, D. R., Fulay, P. P., & Wright, W. J. (2010). The Science and Engineering of Materials, Sixth Edition. Stamford, CT 06902: Cengage Learning.

ASM Handbook. (2000). Mechanical Testing and Evaluation, ASM Handbook Vol. 8. Materials Park, OH 44073-0002: ASM International.

Callister, W. D., & Rethwisch, D. G. (2014). Materials Science and Engineering. New Jersey: John Willey & Sons, Inc.

Gibson, R. F. (2012). Principles of Composite Material Mechanics. Boca Raton, London, New York: CRC Press.

J. P. Anderson, M. C. (2014). Composite laminates fabricated by bladder assisted composite manufacturing (bacm):

JOURNAL OF MATERIALS PROCESSING & CHARACTERIZATION

The effect of AA5083H116 2-layer MIG welding speed on physical and mechanical properties

Mudjijana*
V. Malau
U. A. Salim

Department of Mechanical and Industrial Engineering, Faculty of Engineering, Universitas Gadjah Mada. Jl. Grafika 2, Yogyakarta 55281, Indonesia

Email:
*mudjijana@ugm.ac.id

Keywords
AA5083H116, ER5356, 2-layer MIG (metal inert gas), welding speed, physical and mechanical properties.

Abstract
Metal welding can be performed on 1 layer or more depending on the thickness of the plate welded. In the case of 3-mm-thick plates, high-efficiency welding can be carried out on 1 layer if appropriate welding speed, voltage, and amperage are applied. If two layers are to be used, sound weld of 3-mm-thick plates can be achieved if higher welding speed and lower voltage and amperage are applied. This research was intended to conduct 2-layer MIG weld works at welding speeds of ≥10, 13, and 16 mm/s in accordance with previous research studies and to analyze the physical and mechanical properties generated. This research employed the AA5083H116 material, ER5356 electrode, and argon gas. During the welding processes, the thermal cycles were recorded, and after the processes, the welding results were observed for the macro- and microstructures and for the optimal welding speed under an SEM. In addition, tensile tests, Vickers microhardness tests, and corrosion tests were also undertaken. The results show that the 2-layer MIG welding at the welding speed of 10 mm/s produced the best physical and mechanical properties.

Volume 1, Number 1, 2020, 31-40
DOI: http://dx.doi.org/10.22146/jmpc.v1i1.51417
e-ISSN: 2716-1285, ISSN: 2714-9722

1. Introduction

Welding works are commonplace in the construction sector. With the development of manufacturing process, it is important that welds be carried out in maximum efficiencies. Welding technology is continuously developed to achieve better time and production cost effectiveness. In the transportation sector, specifically, welding applications are ubiquitous in shipping, aviation, and rail transport industries. The materials used can range from carbon steels, aluminum alloys, to stainless steels and a range of other materials. It is imperative to welding constructions that attention be given to the compatibility between the types of materials welded, welding electrodes, and welding methods in order to attain sound welds. A 5083 aluminum alloy is a lightweight metal with a low density of 4.5 g/cm3 (Ashby and Jones, 2012). This material is popular owing to its high tensile strength and corrosion resistance. Yazdipour et al. (2011) conducted an inquiry on MIG welding of AA5083 with a variety of parameters, including welding speeds of 7.24–10 mm/s, voltages of 18–22 V, and electrical currents of 120–182 A, and yielded a maximum ultimate tensile strength value of 337 MPa. Kim et al. in their research (2010) obtained from conventional MIG welding of AA5083H116 a tensile strength value of 344.64 MPa in weld metal, which was higher than that in the base metal, with an efficiency of 85.8%. In a separate study, Li et al. (2017) conducted MIG welding with the ER5356 electrode on two dissimilar metals, 7N01-T5 and 7N01-T4, at varied welding speeds of 6.5, 7.5, and 8 mm/x, electrical current of 290 A, and voltage of 27 V. From that research, they obtained weld-zone tensile strength of 283 MPa, which was lower than that in the BM area (360 MPa for 7N01-T5 and 432 MPa for 7N01-T4). From the results of the corrosion test on the 4.0 M NaCl + 0.5 M KNO3 + 0.1 M HNO3 solution medium it was found that 7N01-T4 was more susceptible to corrosion than 7N01-T5. The part most prone to corrosion was the heat affected zone (HAZ), and in general, the weld metal was more susceptible to corrosion than the base metal. Mudjijana et al. (2017) performed characterization of welds of the AA5083H116 material with the ER5356 electrode at varied MIG welding speeds of 8, 10, and 12 mm/s. It was discovered that at the welding speed of 10 mm/s, the highest tensile strength, bending strength, and welding efficiency were achieved. The results of the studies above can be used as a reference for determination of welding speed for 2-layer MIG welding, with an assumption that the heat generated would be higher than that from 1-layer MIG welding. Thus, it was assumed that the 2-layer MIG welding speed should be faster than that applied in 1-layer MIG welds. This research investigated the effect of ER5356-electrode AA5083H116 2-layer MIG welding speeds (in this study 10, 13, 16 mm/s).

2. Materials and Methods

The material used in this research was AA5093H116 300 mm × 75 mm × 3 mm in size, the electrode used was the ER5356 electrode (ASME, 2001) 0.8 mm in diameter, and the shielding gas used was argon. The welding was undertaken on 2 layers with a Tenjima 200S under the scheme provided in Figure 1 with the welding parameters presented in Table 1. During the welding processes, the thermal cycles were measured with type-K thermocouple wire and an NI USB-9162 instrument in the installation position shown in Figure 2. The welding results were subjected to microstructure observations with a 10% NaOH etching solution (AST, 2015), Vickers microhardness tests with a 100 g load, tensile tests per the ASTM-E8 standard, and corrosion tests with potentiodynamic polarization as shown in Figure 3 within a 3.5% NaCl environment with a specimen thickness of ~2 mm and diameter of ~15 mm. The best welding speed was observed under an SEM (scanning electron microscope).

Table 1. Welding parameters

Welding parameters	
Electrode distance from specimen (mm)	10
Welding speed (mm/s)	10, 13, and 16
Welding angle (θ^o)	80
Average welding voltage (Volt)	19
Average welding current (Ampere)	110
Filler rate (mm/s)	27
Filler diameter (mm)	0.8
Argon flow (liter/minute)	15
Welding 1-2 pause time (s)	15

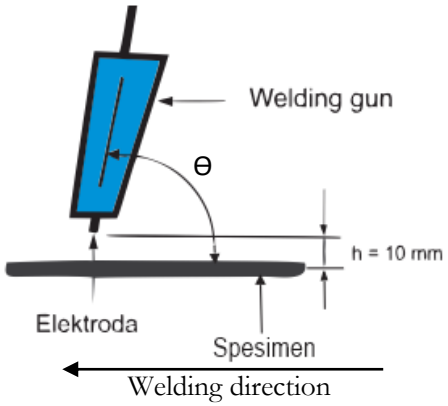

Figure 1. Schematic of welding gun position relative to specimen

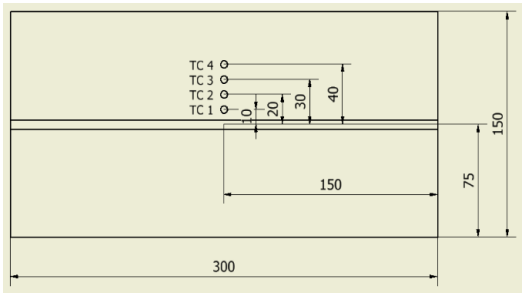

Figure 2. Thermocouple position in specimen

Figure 3. Potentiodynamic polarization corrosion test instrument

3. Results and Discussion

Thermal cycle

Detailed results of the thermal cycle measurement during the welding processes are only provided for the best welding speed of 10 mm/s in Figure 4, while the peak temperatures are presented in Table 2. A sample welding joint generated at the welding speed of 13 mm/s is displayed in Figure 5. The peak TC1 temperatures on layers 1 and 2 at the welding speeds of 10, 13, and 16 mm/s are provided in Table 3. It is shown in the table that the peak temperatures on layer 1 were lower than those on layer 2 because layer 2 had been affected by the initial heating during the welding processes on layer 1 with a pause time of 10 mm/s. The peak temperatures at the welding speed of 10 mm/s were higher than the rest due to bigger heat input based on the equation $Q = VI/v$, where v is welding speed (mm/s), V is welding voltage (Volt), and I is welding current (Amp).

Table 2. Thermal cycle peak temperatures 10 mm from weld line

Welding speed	Temperature (ºC)	
	TC1 peak temperatures on layer 1	TC1 peak temperatures on layer 2
10 mm/s	231.2	244.9
13 mm/s	215.6	241.5
16 mm/s	159.7	183.4

Table 3. Peak temperatures in Figure 4

Specimen	Peak temperatures (°C)			
	TC1	TC2	TC3	TC4
Welding speed of 10 mm/s	231.2	151.1	109.5	97.4
	244.9	172.1	133.5	120

Macro- and micro observation

Macrostructure observation was carried out under a 10× magnitude optical microscope (OM), and the microstructure observation a 200× magnitude optical microscope. The macrostructure observation results in Figure 6 show the differences between the weld zones of base metal (BM), heat affected zone (HAZ), and weld metal (WM). The weld metal was rich in porosity in all specimens. Porosity is a weld defect from the presence of entrapped solved hydrogen during the welding process in the molten metal, where the molten metal freezes before the hydrogen gets to evaporate. It could also be observed that the specimen welded at the speed of 16 m/s experienced incomplete penetration, which is presumed to happen due to a number of factors, namely excessively low welding current, excessively fast welding speed, improper torch angle, and poor welding preparation.

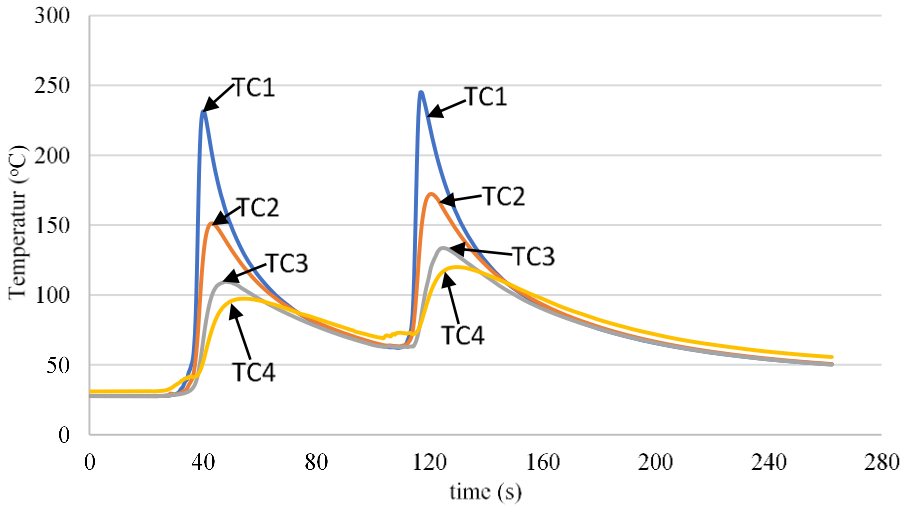

Figure 4. Thermal cycles at welding speed of 10 mm/s

Figure 5. Welding result at welding speed of 13 mm/s

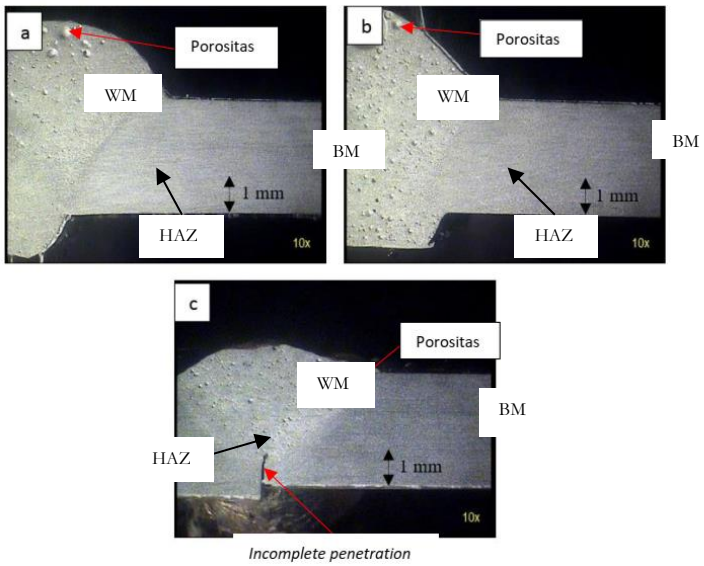

Figure 6. Sectional macrostructure at welding speeds: (a) 10 mm/s, (b) 13 mm/s, and (c) 16 mm/s

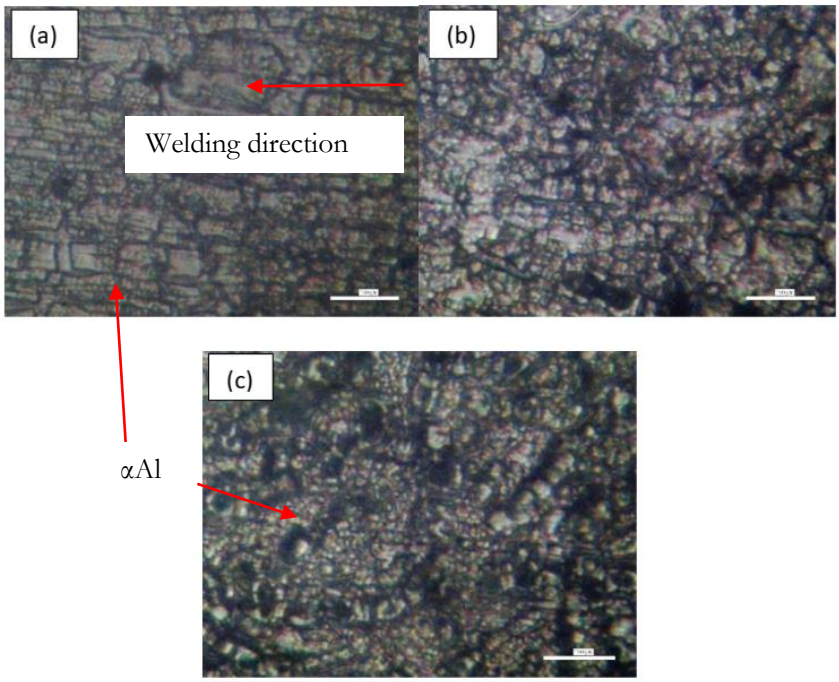

Figure 7. Macrostructure in (a) base metal (BM), (b) heat affected zone (HAZ), and (c) weld metal (WM) at welding speed of 10 mm/s.

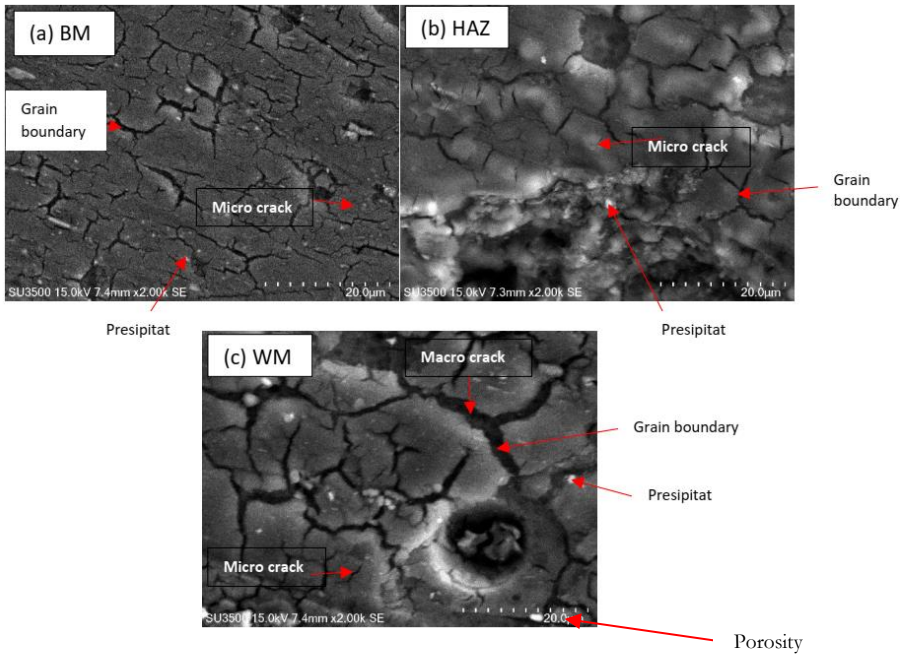

Figure 8. Microstructure under scanning electron microscope (SEM): (a) BM, (b) HAZ, and (c) WM

Microstructure imaging was performed in three different regions, namely base metal (BM), heat affected zone (HAZ), and weld metal (WM), and only the images for the welding speed of 10 mm/s are displayed because the microstructures at the other welding speeds were similar with distinction only in the grain size. The grain size at the welding speed of 10 mm/s was bigger than those at the welding speeds of 13 and 16 mm/s owing to larger heat input. The results of the microstructure observation at the welding speed of 10 mm/s are shown in Figure 7. As exhibited in Figure 7(a), the microstructure in the BM had elongated grains from fabrication with H116 treatment. The BM microstructure was unaffected by the heat produced by the welding process. The HAZ microstructure shown in Figure 7(b) had grains partially similar to those in the BM and partially equiaxed due to WM-BM fusion. Meanwhile, the microstructure in the WM region was almost entirely equiaxed. The αAl appeared white in color for an Al-Mg alloy with an Mg content for AA5083H116 of roughly 4.5%.

The results of the SEM microstructure observation at the welding speed of 10 mm/s are shown in Figure 8 ((a) BM, (b) HAZ, (c) WM). From the SEM results, it can be observed that the grains in the BM were smaller in size than those in the HAZ and WM due to H116 treatment. In the HAZ, the granular sizes were slightly bigger than those in the BM, yet slightly smaller than those in the WM, from heat influence over the welding process. On the other hand, the WM had grains in the largest sizes and in equiaxed shapes; the WM was the ER5356 welding material with air cooling-freezing rate. Microcracks and precipitates were spotted in all the BM, HAZ, and WM. Microcracks in the BM emerged because the H116 treatment performed involved solid solution treatment and rolling up to ¾ hardness. The microcracks in the HAZ were caused by uneven cooling process and non-uniform fusion zone unlike the BM. Meanwhile, the microcracks in the WM were brought about by both small and big grain sizes which caused imbalance in the cooling rate. It is noticeable

at the granular boundary that more macrocracking took place than microcracking.

Vickers hardness

Based on Figure 9, Table 3, and Figure 10, the hardness values in the BM from the testing were virtually uniform across the three specimens. The specimen for the welding speed of 10 mm/s yielded an average hardness value of 94.07 VHN, 13 mm/s 93.10 VHN, and 16 mm/s 93.79 VHN. The average hardness value in the HAZ was the highest in the 16 mm/s welding speed specimen, namely 92.21 VHN. In the 13 mm/s welding speed specimen the average value was 83.11 VHN, while 10 mm/s 77.34 VHN. The WM did not exhibit any significant difference in the hardness value between welding speeds. The specimen for the welding speed of 16 mm/s had the highest average hardness value of 72.96 VHN, followed by those for the welding speeds of 13 mm/s and 10 mm/s with 70.94 VHN and 69.84 VHN, respectively.

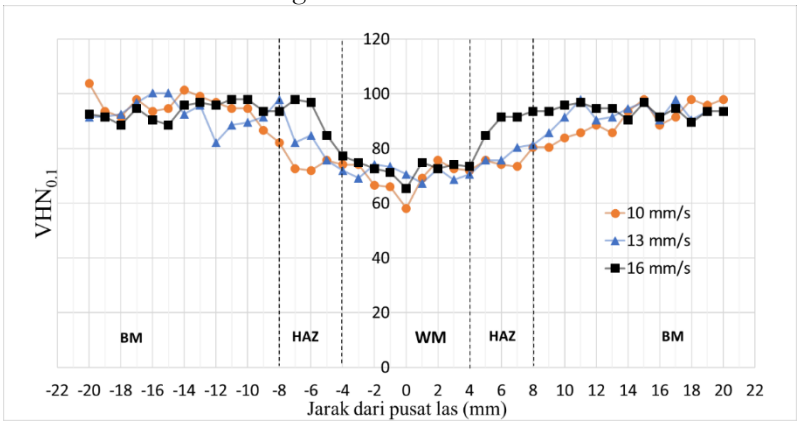

Figure 9. Hardness value comparison

Table 4. Average hardness values

Welding speed	BM	HAZ	WM
	Average Vickers hardness value		
10 mm/s	94.07	77.34	69.84
13 mm/s	93.10	83.11	70.94
16 mm/s	93.79	92.21	72.96

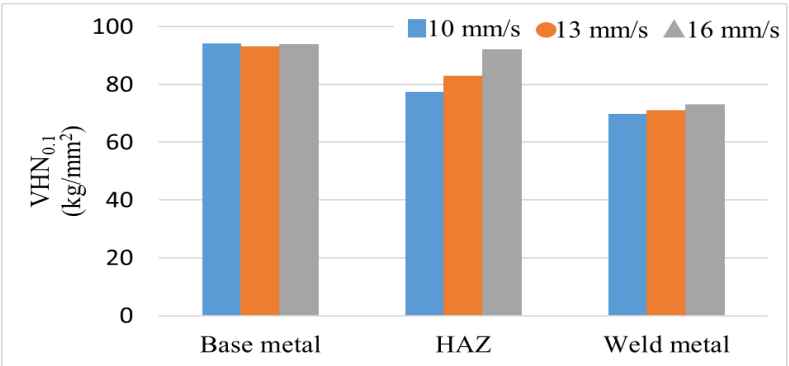

Figure 10. Comparison of average hardness values in BM, HAZ, and WM

In Figure 10 it can be observed that the Vickers hardness value-distance to weld core curve for every weld variation had a similar trend line to another variation. The lowest hardness values were found in the WM, which increased in the HAZ and achieved maximums in the BM. The HAZ exhibited lower hardness values than the BM. Series 5xxx aluminum alloys are non-heat treatable, thus the strength cannot be increased by applying heat. The decrease in hardness value in the HAZ can be associated with microstructure. The HAZ had bigger grains than the BM, causing the strength to withstand dislocation to go down. The lowest hardness value in the WM, too, is tied to microstructure. Compared to the BM and HAZ, the WM had larger granular sizes giving it the lowest strength to withstand dislocation. The 16 mm/s welding speed specimen, which received the smallest heat input, yielded the highest hardness value, while the 10 mm/s welding speed specimen, which received the most heat input, did the lowest hardness value. Series 5xxx aluminum alloys can be subjected to work hardening, which can cause alteration to the microstructure. A rolling or work hardening process is a key factor that gives the BM greater hardness than the WM (Yazdipour dkk, 2011).

Tensile Test

The results of the tensile test per the ASTM-E8 are provided in Figure 11. The yield strength value of 292.52 MPa and tensile strength value of 360.31 MPa of the raw material were to be compared with the yield and tensile strength of the 2-layer MIG weld specimens. At the welding speed of 10 mm/s, the specimen had the greatest yield strength and tensile strength (230,95 Mpa and 281.07 MPa, respectively), thus the maximum welding efficiency (welding efficiency = the tensile strength of the welded material divided by the tensile strength of the raw material = 78%). The specimens at the welding speeds of 13 mm/s and 16 mm/s had lower yield strength and tensile strength (Figure 11). The 2-layer MIG welding efficiency was indistinct from that of 1-layer MIG welding as studied by Mudjijana et al. (2017). Hence, the plate thickness of 3 mm is not suited for 2-layer welding.

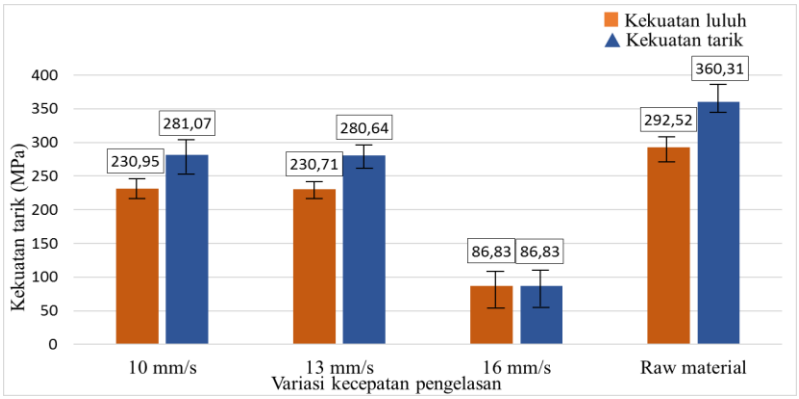

Figure 11. Tensile strength vs welding speed variation

Potentiodynamic polarization corrosion test

The results of the corrosion test with the potentiodynamic polarization method (potential (V) vs current density comparison (A/cm^2)) are presented in Figure 12. Through calculations, corrosion rates were obtained and are presented in Table 4. BM had the

lowest corrosion rate, namely 0.253 mm/year. The specimen for the welding speed of 10 mm/s produced a corrosion rate of 0.285 mm/year, 13 mm/s 0.277 mm/year, and 16 mm/s 0.450 mm/year.

The corrosion rate in the weld zone was higher than the base material, in which case, the corrosion rate in the weld zone would increase with welding speed. Al-Mg alloys have good resistance to corrosion (Wiryosumarto, 2000). Variation in heat input amount leads to variation in precipitate amount in WM, while variation in precipitate variation leads to variation in Ecorr and Icorr values in WM. The more precipitate amount in WM, the higher the Ecorr and Icorr values and the faster the corrosion rate. A defect in WM in the form of porosity also plays a role in the acceleration of the corrosion rate. Corrosion will attack the weakest region in which defects are found. Varying corrosion resistance rates across weld joint locations are dependent on the distribution, sizes, and types of precipitates and the chemical composition (Li et al., 2017).

Table 5. Corrosion rates of BM and 2-layer MIG welding result

Material	Welding speed (mm/s)	E_{corr} (mV)	I_{corr} (μA)	Corrosion rate (mm/ year)
Base material	-	-743.14	22.34	0.25
Weld zone	10	-733.91	25.12	0.29
	13	-751.42	33.23	0.38
	16	-759.60	39.70	0.45

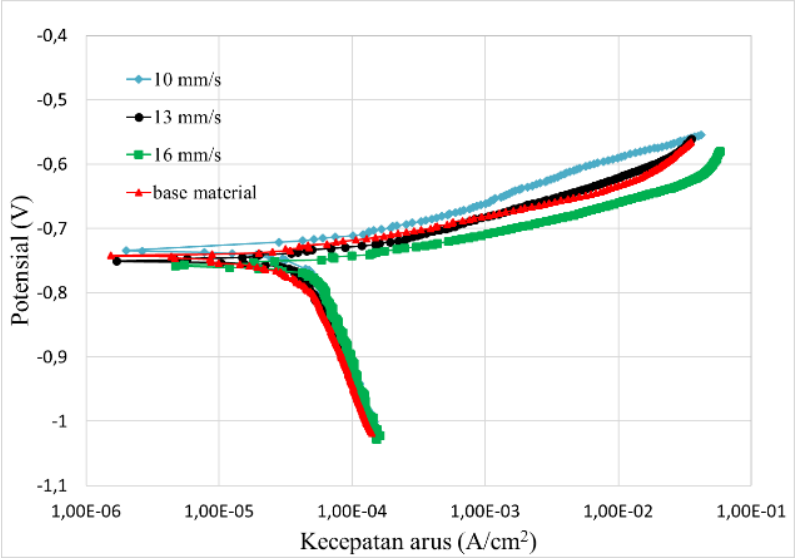

Figure 12. Potential (V) vs current density (A/cm²)

4. Conclusion

Based on the testing on the 2-layer MIG welding joints obtained at different welding speeds (10, 13, 16 mm/s), it can be concluded that (1) an increase in the welding speed causes a decrease in the maximum temperature achieved, leading to lowered heat input received by the specimen and lowered tensile strength; (2) an increase in the welding speed causes an increase in the hardness in the HZ and BM; and (3) an increase in the welding speed causes a decrease in the resistance to

corrosion in the weld zone, in which case, the BM has better corrosion resistance than the WM.

5. Acknowledgements

Gratitude is due to the Minister of Research, Technology, and Higher Education, who have funded this research under the UGM PDD contract no. 1769/UN1/DITLIT/DIT-LIT/LT/2018, the Department of Mechanical and Industrial Engineering of the Faculty of Engineering, UGM, for the opportunity, and Mr. Ekak, Mr. Sunhaji, Mr. Yasin, and Mr. Arief, for assisting with this research.

6. References

Ashby, M. F. dan Jones, D. R. H., 2013, Engineering Materials 2: An Introduction Microstructures and Processing, 4thed, Butter-worth-Heinemann, p. 190.

ASME, 2001, Materials Part C – Specifications for Welding Rods, Electrodes, and Filler Metals, ASME, New York.

ASTM, 2009, E8/E8M-09, Standard Test Method for Tension Testing of Metallic Materials, ASTM International.

ASTM, 2015. E407-07 (Reapproved 2015), Standard Practice for Micro-etching Metals and Alloys, ASTM International.

Haelsig, A., Kusch, M., Mayr, P., 2012, New Findings on The Efficiency of Gas Shielded Arc Welding. 56, pp. 98-104.

Kim, S-J., Kim, S-K., Park, J-C., 2010, The Corrosion and Mechanical Properties of Al Alloy 5083-H116 in Metal Inert Gas Welding Based on Slow Strain Rate Test. Surface & Coatings Technology, 205, pp. S73–S78.

Li, S., Dong, H, Shi, L., Li, P., Fe., Y. 2017, Corrosion Behavior and Mechanical Propertieso of Al-Zn-Mg Aluminum Alloy Weld, Corrosion Science, 123, pp. 243–255.

Mudjijana, Ilman, M.N., Iswanto, P.T., 2017, Karakterisasi Pengaruh Kecepatan Las pada Pengelasan MIG AA 5083 H116 dengan Elektroda ER 5356, POROS, Volume 15 Nomor 1, pp. 26-34.

Wiryosumarto, H., 2000, Teknologi Pengelasan Logam, PT Pradnya Paramita, Jakarta.

Yazdipour, A.R., Shafiei, L., Aval, H.J., 2011, An Investigation of The Microstructures and Properties of Metal Inert Gas and Friction Stir Welds in Aluminum Alloy 5083, Sadhana, Vol. 36, pp.50

JOURNAL OF MATERIALS PROCESSING & CHARACTERIZATION

A Preliminary Study of Extraction and Characterization of Nanocrystalline Cellulose (NCC) from Ramie Fiber

Kusmono*
M.W. Wildan
M.N. Ilman

Department of Mechanical and Industrial Engineering, Faculty of Engineering, Universitas Gadjah Mada. Jl. Grafika 2, Yogyakarta 55281, Indonesia

Email:
*kusmono@ugm.ac.id

Keywords
nanocrystalline cellulose, ramie fiber, chemical treatment, crystallinity index, thermal stability.

Abstract
Nanocrystalline cellulose (NCC) is today's one of rapidly growing nanocomposite reinforcing materials. This is thanks to some advantages that come with it over anorganic nanocomposite reinforcing materials, for example, nanoclay, nanosilica, nanoalumina, carbon nanotubes, among others. Some of the advantages of NCC are environment-friendliness due to being organic-compound-based, high mechanical property, and easy manufacturing. NCC can be extracted from natural cellulose sources, such as natural fiber, wood, and animals. One of the natural fibers rich in cellulose content, in this case around 80%, is fiber of ramie which is ubiquitous in Indonesia. It is well known that the acid hydrolysis method is an easy route to NCC fabrication. A number of chemical treatments like de-waxing, bleaching, and alkaline treatment are typically performed prior to acid hydrolysis process. The effect of such chemical treatments as precursors of alkaline hydrolysis on ramie fiber characteristics was investigated in this research. Firstly, ramie fiber was cut 1 cm in size, then grinded and sieved. The fiber was then subjected to de-waxing process by adding it into a toluene-ethanol solution (1:2). Then, it was submitted to bleaching with 0.7% sodium chlorite (NaClO2) solution at 75 °C for 1 hour. Lastly, the fiber was subjected to an alkaline treatment in 2% NaOH solution for 2 hours. Characterization with FT-IR, XRD, and TGA of the fiber which had underwent a number of surface treatments was conducted. Results show that the chemical treatments had successfully removed amorphous components like lignin and hemicellulose from the ramie fiber. Chemical treatments were proven able to increase the crystallinity index and thermal stability of ramie fiber.

Volume 1, Number 1, 2020, 41-45
DOI: http://dx.doi.org/10.22146/jmpc.v1i1.51418
e-ISSN: 2716-1285, ISSN: 2714-9722

1. Introduction

Nanocrystalline cellulose (NCC) is a nano-scale, needle-like cellulose material 5–10 nm in diameter and 100–500 nm in length which is synthesized from a cellulose source (Kian et al., 2018). NCC is a promising organic nanoparticle material with several unique properties, including nano-scale size, high specific strength and modulus, high surface area, high crystallinity and unique optical properties, high crystallinity index, ultra light weight, and environment-friendliness (Csiszar et al., 2016; Ngwabebhoh et al., 2018). The NCC material has a range of potential applications in various fields, for example, medical, optical, and nanocomposite material applications (Li et al., 2012).

The acid hydrolysis method is the most widely used natural-cellulose-based NCC manufacturing method (Habibi et al., 2010). Included in natural celluloses are natural and marine animal fibers. Sulfuric acid at a concentration of 60–70% and temperature of 45 °C and hydrolysis time of around few minutes up to several hours have also been frequently used in acid hydrolysis processes (Jonoobi et al., 2015). Acid hydrolysis can remove amorphous components (e.g., wax film, hemicellulose, lignin) from natural fibers.

Ramie fiber is a natural fiber derived from ramie plants abundant in Indonesia. It contains relatively high cellulose (80–85 wt%) and high mechanical property. By far, ramie fiber applications are still confined to rod materials, gunny sacks, fabric or paper materials, and microcomposite reinforcement. Thus, it is of considerable interest if a research study is performed on NCC fabrication from high-cellulose ramie fiber. NCC extraction and characterization studies have been performed by some previous researchers using a variety of natural cellulose sources, for example, bamboo (Brito et al., 2012), straw (Lu and Hsieh, 2012), palm tree (Ilyas et al., 2018), and so forth. Ramie-sourced NCC extraction and characterization research is still rare, leading to the need for conducting a study on NCC fabrication from ramie fiber.

Before acid hydrlysis process, some chemical treatments for ramie fiber purification like de-waxing, bleaching, and alkiline treatment were carried out. The results of the ramie fiber characterization past the chemical treatments (de-waxing, bleaching, alkali) are reported in this paper. The characterization was conducted with FT-IR, XRD, and TGA.

2. Methodology

Ramie fiber was cut 1 cm in size, grinded, and sieved to pass 40 mesh. Then, the fiber was de-waxed in a solution of a mixture of toluene and ethanol (2:1) using Soxhlet. Afterwards, the fiber was washed in alcohol and water, then dried at 80 °C for 2 hours.

In the next step, the fiber was bleached at 75 °C for 1 hour in a 0.7% sodium chlorite ($NaClO_2$) solution and added with acetic acid until pH 4. The fiber-to-solution ratio was 1:100 (w/v). The fiber then rinsed in distilled water until the pH became normal and oven-dried at 80 °C for 2 hours. The bleaching result was submitted to alkalization with 2% NaOH solution at 95 °C for 2 hours, then rinsed and dried. Afterwards, the ramie fiber was subjected to characterization using FT-IR, XRD, and TGA. In addition, the untreated ramie fiber chemical composition was also tested using standard gravimetry.

3. Results and Discussion

From the untreated ramie fiber chemical composition test, it was found that the ramie fiber contained 86.38% holocellulose, 72.68% α-cellulose, and 0.48% lignin, indicating that ramie fiber does contain very high cellulose and low lignin. From the results, it can be concluded that the rich cellulose content in ramie fiber causes it to be highly crystalline. Thus, the potential for nanocrystalline cellulose (NCC) manufacturing from ramie fiber cellulose source is enormous.

Figure 1 shows the FT-IR spectra for the fiber before and after de-waxing, bleaching, and alkaline treatment. The figure reveals that the ramie fiber both before and

after chemical treatments had the same peaks: 3,464 cm^{-1}; 2,931 cm^{-1}; 2,368 cm^{-1}; 1,751 cm^{-1}; 1,643 cm^{-1}; and 1,064 cm^{-1}. The peak 3,464 cm^{-1} shows the characteristic of the hydroxyl group –OH in cellulose, hemicellulose, and lignin. The peak 2,931 $cm^{°°-1}$ shows the characteristic of the methyl and methylen of C–H stretching. The peak 2,368 cm^{-1} indicates the acetyl group of C–O stretching, while the peak 1,751 cm^{-1} the carboxylic group C=O in hemicellulose and pectin. The peak 1,643 cm^{-1} indicates the C=C group in lignin. The peak 1,435 cm^{-1} indicates the characteristic of the –CH3 group, while the peak 1,064 cm^{-1} shows the acetyl group C–O in lignin. The FT-IR results also show that the peak 1,751 cm^{-1} which is characteristic of the C=O group in hemicellulose and pectin in untreated ramie fiber did not show up after de-waxing, bleaching, and alkaline treatments. It can be concluded that surface chemical treatments had successfully solved the amorphous components in fiber like wax, hemicellulose, and pectin.

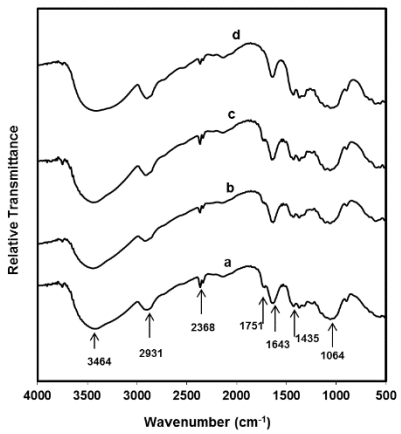

Figure 1. FT-IR of ramie fiber powder: a.untreated; b. de-waxing; c. Bleaching; d. Alkali

The CRD patterns of ramie fiber before and after chemical treatments are presented in Figure 2. It can be seen that three samples (before, after alkaline treatment, and after Soxhlet treatment) exhibited 3 same peaks, namely about 2θ = 18, 22, and 35°. All the peaks show the crystalline structure of cellulose 1, which were determined as crystal fields (10Ī), (002), and (040). Then, from the XRD patterns, the crystallinity index was calculated by referring to Segal's equation (Segal et al., 1959), and the results are recorded in Table 1. The crystallinity index of the fiber before treatment was 79.75%, after de-waxing 85.63%, after bleaching 85.50%, and after alkaline treatment 86.68%. From these results, it can be concluded that chemical treatments (de-waxing, bleaching, and alkali) had increased the crystallinity index of the ramie fiber. The crystallinity index rise is related to the dissolution of some amorphous components like hemicellulose, lignin, pectin, and wax film and to the readjustment of the crystal area. De-waxing is a treatment for removing the wax film in ramie fiber, bleaching for lignin, and alkaline treatment for hemicellulose component.

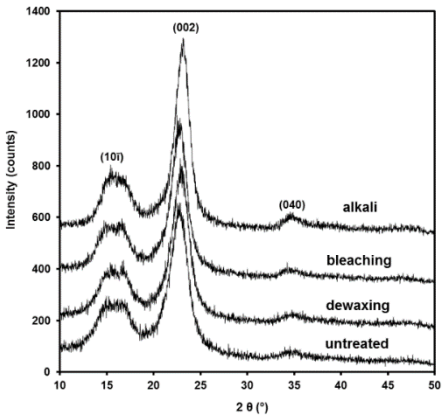

Figure 2. XRD patterns of ramie fiber powder

Table 1. Crystallinity index of ramie fiber powder

Specimen	Crystallinity index (%)
untreated	79.75
de-waxing	85.63
bleaching	85.50
alkali	86.68

The thermal stability of the ramie fiber before and after chemical treatments were studied using a thermogravimetric analysis (TGA), and the results are shown in Figure 3. From the figure it can be observed that the four samples (untreated, de-waxing, bleaching, and alkali) exhibited 2 identical

degradation stages, namely at 30–100 °C and 200–350 °C. The first degradation is related to water evaporation within the fiber (al-Dulaimi and Wanrosli, 2017; Liu et al., 2017). Water evaporation in untreated fiber ended at relatively higher temperature than the treated fiber. This is because the water content absorbed in the untreated fiber was higher than that in the treated one (Ilyas et al., 2018). The reason is that the hemicellulose content in the treated fiber had declined from the chemical treatment. Hemicellulose is a component in fiber that has a high water absorption property. Figure 3 also suggests that the temperature at which 10% weight loss happened was the highest in the fiber after alkaline treatment, followed by the bleached, de-waxed, and untreated one. This also proved that chemical treatments in ramie fiber can improve the thermal stability. This is in agreement with the FT-IR results that hemicellulose would disappear after alkaline treatment. The second degradation took place at 200–350 °C. This is linked to the decomposition/degradation of the hemicellulose and cellulose components (Ishak et al., 2012).

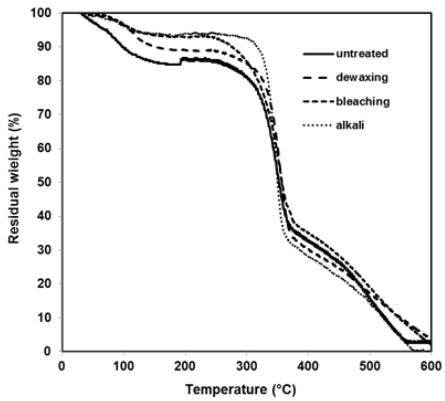

Figure 3. TGA curve of ramie powder

4. Conclusion

Based on the FT-IR and XRD analyses results, it can be concluded that chemical treatments (de-waxing, bleaching, and alkali) in ramie fiber had successfully removed hemicellulose component, wax film, and lignin and in turn improve the crystallinity index. Besides, chemical cyrstallinity had been able to improve the thermal stability of ramie fiber.

5. Acknowledgments

This research was funded by the 2018 Grant of the Department of Mechanical and Industrial Engineering, Faculty of Engineering, UGM (No. 809/H1.17/TMI/LK/2018) and the 2018 Basic Higher Education Distinguished Research Grant (PDUPT) of the Institute for Research and Community Service (LPPM) of UGM (No. 110/UN1/DITLIT/DIT-LIT/LIT/2018). The authors would like to thank Faiz Listyanda and Dimas Abdillah Akbar for the assistance in data collection.

6. References

L.K. Kian, M. Jawaid, H. Ariffin, Z. Karim, 2018, Isolation and characterization of nanocrystalline cellulose from roselle-derived microcrystalline cellulose, International Journal of Biological Macromolecules, Vol. 114, 54-63.

E. Csiszar, P. Kalic, A. Kobol, E.P. Ferreira, 2016, The effect of low frequency ultrasound on the production and properties of nanocrystalline cellulose suspensions and films, Ultrasonics Sonochemistry, Vol. 31, pp. 473–480.

F.A. Ngwabebhoh, A. Erdem, U. Yildiz, 2018, A design optimization study on synthesized nanocrystalline cellulose, evaluation and surface modification as a potential biomaterial for prospective biomedical applications, International Journal of Biological Macromolecules, Vol. 114, pp. 536–546.

W. Li, J. Yeu, S. Liu, 2012, Preparation of nanocrystalline cellulose via ultrasound and its reinforcement capability for poly (vinyl alcohol) composites, Ultrasonic Sonochemistry, Vol. 19, pp. 479-485.

Y. Habibi, L.A. Lucia, O.J. Rojas, Cellulose nanocrystals: chemistry, selfassembly, and applications, Chem. Rev. 110 (2010) 3479–3500.

M. Jonoobi, R. Oladi, Y. Davoudpour, K. Oksman, A. Dufresne, Y. Hamzeh, R. Davoodi, 2015, Different preparation methods and properties of nanostructured cellulose from various natural resources and residues: a review, Cellulose, Vol. 22, 935-969.

B.S. L. Brito, F.V. Pereira, J.L. Putaux, B. Jean, 2012, Preparation, morphology and structure of cellulose nanocrystals from bamboo fibers, Cellulose, Vol. 19, pp.1527–1536.

P. Lu, Y.L. Hsieh, 2012, Preparation and characterization of cellulose nanocrystals from rice straw, Carbohydrate Polymers, Vol. 87, pp. 564– 573.

R.A. Ilyas, S.M. Sapuan, M.R. Ishak, 2018, Isolation and characterization of nanocrystalline cellulose from sugar palm fibres (Arenga Pinnata), Carbohydrate Polymers, Vol. 181, pp. 1038-1051.

L. Segal, J.J. Creely, A.E. Martin, C.M. Conrad, 1959, An empirical method for estimating the degree of crystallinity of native cellulose using the X-Ray diffractometer. Textile Research Journal, Vol. 29(10), pp. 786–794.

A. A. Al-Dulaimi, W.D. Wanrosli, 2017, Isolation and Characterization of Nanocrystalline Cellulose from Totally Chlorine Free Oil Palm Empty Fruit Bunch Pulp, Journal of Polymers and the Environment, Vol. 25, pp.192-202.

Z. Liu, X. Li, W. Xie, H. Deng, 2017, Extraction, isolation and Characterization of Nanocrystalline Cellulose from Industrial Kelp (Laminaria Japonica) waste, Carbohydrate Polymers, Vol. 2017, pp. 353-359.

M. R. Ishak, S.M. Sapuan, Z. Leman, M.Z.A. Rahman, U.M.K. Anwar, 2012, Characterization of sugar palm (Arenga Pinnata) fibres. Journal of Thermal Analysis, and Calorimetry, Vol. 109(2), 981–989.

JOURNAL OF MATERIALS PROCESSING & CHARACTERIZATION

The Effects of Withdrawal Stop Duration in the Directional Solidification of Al-7 wt% Si Alloy on Solidification Parameters, Microstructure, and Microhardness

[1]S. Piseth
[2]D. Masnur

[1]Department of Industrial and Mechanical Engineering, Faculty of Electrical Engineering, Institute of Technology of Cambodia, Russian Federation Boulevard P.O. BOX 86 Phnom Penh, Cambodia

[2]Mechanical Engineering Department, University of Riau, Kampus Bina Widya km 12.5 Simpang Baru, Pekanbaru 28293, Indonesia

Email: [1]pisethseab@gmail.com

Keywords
Aluminum alloys, Dendrite growth, Directional solidification, Withdrawal.

Abstract
The effects of withdrawal stop duration in the directional solidification of Al-7 wt% Si alloy on solidification parameters, microstructure, and microhardness were investigated. Directional solidification experiments were carried out in five stopping durations: 0 s, 20 s, 30 s, 40 s, and 50 s. Some solidification parameters such as growth rate and temperature gradient were calculated in the stopping region 15 mm from the bottom of the sample. Microstructure parameters such as primary and secondary dendrite arm spacings were defined on both longitudinal and transverse sections in the stopping region, whereas microhardness properties were tested on the longitudinal section in this region. With the rise in the withdrawal stop duration from 0 s to 50 s, the growth rate decreased slightly from 1.26 to 0.84 mm/s, while the temperature gradient remained at 1.71 °C/mm. Furthermore, the microstructure of α-Al dendrites became coarser, and their shapes changed from thin to irregular plates. Primary and secondary dendrite arm spacings increased from 106.4 to 205.7 μm and 19.4 to 38.1 μm, respectively, when the stopping duration was increased. In addition, the hardness decreased from 54.0 to 49.9 HV.

Volume 1, Number 1, 2020, 47-56
DOI: http://dx.doi.org/10.22146/jmpc.v1i1.52249
e-ISSN: 2716-1285, ISSN: 2714-9722

1. Introduction

Aluminum-silicon alloys are the most important among cast alloys, and they have widespread applications especially in the aerospace and automotive industries. They exhibit excellent fluidity, castability, corrosion resistance, low specific gravity, high coefficients of thermal expansion, high wear resistance , moderate strength, high ductility, reduced cracking, and improved feeding in the minimization of shrinkage porosity during solidification. Casting in a directional solidification process is critical in the evolution of microstructure. It has been noted that in some applications such as semiconductors, solar cells, heat and fluid flow equipment, the cellular or dendritic microstructure direction affects the efficiency. The best conductibility in heat transfer applications is exhibited in the unidirectional microstructure. Meanwhile, a unidirectional crystal orientation in hypoeutectic Al-Si alloys can be achieved when the alloys contain 5–10 wt% of Si.

Withdrawal rate is the rate of the rod bar in a Bridgman furnace. It is the main parameter affecting the microstructure of a metal alloy during a solidification process. Vibration or change in withdrawal rate affects solidification parameters. To understand the mechanism of solidification, solidification parameters such as temperature gradient (G) and growth rate (V) should be controlled. Meanwhile, microstructure parameters such as primary dendrite arm spacing (PDAS) and secondary dendrite arm spacing (SDAS) determine the mechanical properties of the material. The hardness of the material or alloy depends on the grain size or lamellar spacing: the smaller the lamellar spacing, the higher the hardness.

Thus, in the present work, an attempt was made to investigate the effects of withdrawal stop duration in the directional solidification of Al-7 wt% Si alloy on solidification parameters, microstructure, and microhardness. We will also briefly discuss the relationships between growth rate, dendrite arm spacing (DAS), and microhardness.

2. Materials and Methods

2.1. Materials

High-purity Al (99.95 wt%) and Al-15 wt% Si master alloy were weighted and melted in an electric furnace to prepare a new master alloy composition with 7 wt% Si. The raw materials and samples were analyzed by Thermo Scientific™ ARL iSpark™ OES to ensure their chemical composition. The chemical composition of the alloy is shown in Table 1.

Table 1. Chemical Composition of the Samples

Element	Al	Si	Fe	Other
wt. %	92.54	7.00	0.32	±0.01

2.2. Directional Solidification Method

The directional solidification of the sample alloy was performed in a Bridgman-type directional solidification furnace. The experimental apparatus is schematically shown in Figure 1. The detail of the Bridgman-type furnace is shown in Figure 2. Using the Bridgman method, molten alloy was poured into a clay mold (60 mm in length, 6 mm in internal diameter, and 10 mm in external diameter). There were six holes along the mold into which K-type thermocouples were inserted to measure the temperatures during melting and freezing. The thermocouples were mounted at T_1 = 5 mm, T_2 = 15 mm, T_3 = 25 mm, T_4 = 35 mm, T_5 = 45 mm, and T_6 = 55 mm from the bottom of the clay mold (see in Figure 3a). The temperature data were recorded by a data-logger and transferred to a computer (see in Figure 1).

The samples making was through two processes. Firstly, the aluminum-silicon alloy was melted in the electric furnace at 700 °C. The molten alloy was poured into a permanent mold (PM) to fabricate cylindrical samples with dimensions of 6 mm in diameter and 60 mm in length. Before the pouring, the carbon steel mold was pre-heated to around 150 °C. A resulting PM sample is shown in Figure 3b. Secondly, The PM samples were re-melted in the Bridgman-type solidification

apparatus. To ensure that the temperature in the furnace was uniform, the temperature of 700 ˚C at which the samples were melted was held for around 30 minutes. In this process, the samples were pulled down by a synchronous motor at a constant withdrawal rate of 16.433 μm/s. The samples were quenched for 35 s at a constant flow rate during the downward movement, and then the motor was stopped for durations of 0 s, 20 s, 30 s, 40 s, and 50 s. Past each of the stopping durations above, the motor was moved downward again until outsize of furnace. One of the products of the directional solidification is shown in Figure 3c.

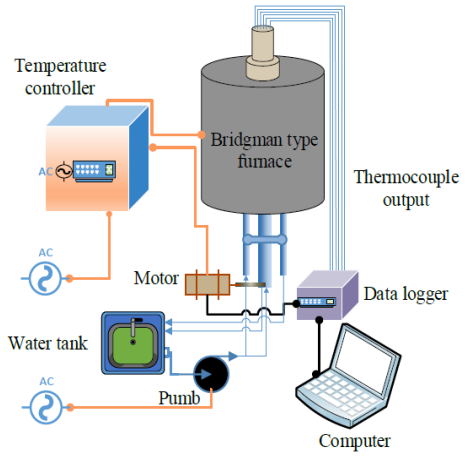

Figure 1. Bridgman-type directional solidification experimental system and equipment

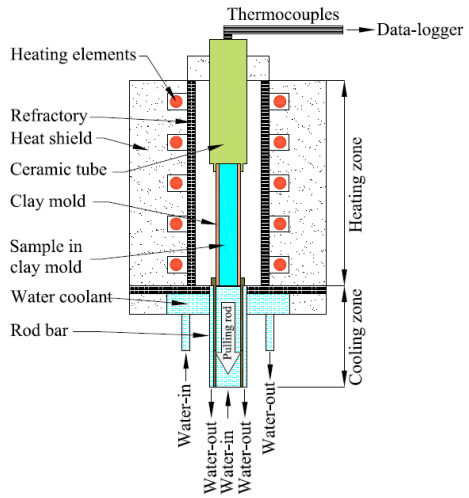

Figure 2. Details of Bridgman-type directional solidification furnace

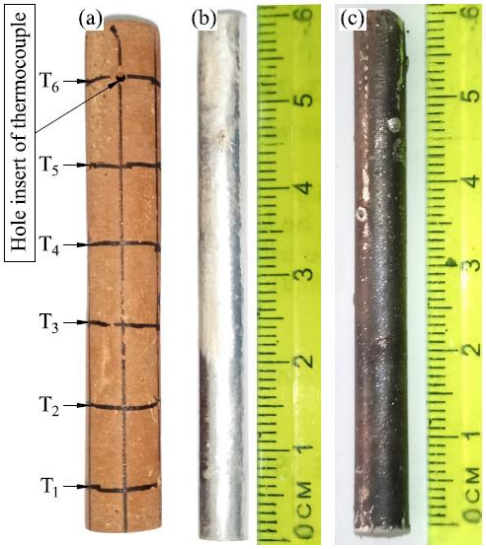

Figure 3. Sample and mold: (a) clay mold; (b) PM sample; (c) directional solidification sample

2.3. Calculation of Solidification Parameters

Solidification parameters such as temperature gradient and growth rate were calculated based on temperature, solidification time, and thermocouple distance between T_2 and T_5. Those positions were selected based on the estimation of the region of dendrites growth between the minimum and the maximum during the withdrawal stop duration. The thermocouple distances are shown in Figure 3a. T_2 is the temperature of the second thermocouple at the solid-liquid interface, T_5 is the temperature of the fifth thermocouple in a liquid phase, and ΔT is the temperature difference between T_2 and T_5. The thermocouple distance from X_2 to X_5 is ΔX. Temperature gradient is defined by the ratio of ΔT to ΔX ($G=\Delta T/\Delta X$), whereas growth rate (V) is calculated by the formula $V=\Delta X/\Delta t$. Δt is the time taken to reach the solid-liquid interface from T_2 to T_5 [11]–[13].

2.4. Microstructure Observation

The quenched samples were cut along the longitudinal and transverse axes. Those sections were cold-mounted with epoxy-resin and then mechanically wet-ground with SiC paper to 5,000 grit. After

polishing, those sections were etched with NaOH solution for 2–3 s (95 ml H_2O and 10 g NaOH) for metallographic observation.

The microstructure in both longitudinal and transverse sections was photographed with an Olympus C-35AD-4 microscope camera bottom up at the same magnification.

2.5. Measurement of Microstructure Parameters

PDAS and SDAS were measured in the stopping region using the ImageJ 1.52i software [14]. In this section, the simple method was used to calculate the SDAS [15] using the formula $SDAS = L/(n-1)$, where L is dendrite length and n is the total number of secondary dendrites.

2.6. Microhardness Testing

The hardness of the samples on the longitudinal section was monitored by the Boehler Vickers hardness testing machine. The monitoring was carried out with a load of 50 g and a loading duration of 10 s. The samples were evaluated in the stopping region 15 to 50 mm from the bottom.

3. Results and Discussions

3.1. The Effects of Withdrawal Stop Duration on Solidification Parameters

Figure 4 shows the growth rates which varied with stopping duration, and Figure 5 the temperature gradient values which varied with stopping duration. The growth rate fell slightly from 1.26 to 0.84 mm/s when the stopping duration was increased from 0 s to 50 s. On the other hand, the average values of temperature gradient in various stopping durations were highly similar (see in Figure 5). The maximum value was 1.82 °C/mm, achieved in the stopping duration of 20 s, and the minimum value was 1.61 °C/mm, achieved in the stopping duration of 0 s. The temperature gradient values were not significantly different. Thus, it can be assumed that the temperature gradient was constant. Throughout the stopping durations of 0 s to 50 s in the directional solidification process, the temperature gradient did not change significantly, with an average value of 1.71 °C/mm. According to these results, the temperature difference between T_2 and T_5 was very small despite the stopping duration increase. The rod bar in the Bridgman-type furnace pulled the samples downward during the process from the heating to the cooling zones. In this situation, the sample of a longer withdrawal stop duration had a slower growth rate than that of a shorter one. These results show that withdrawal stop duration would affect other parameters such as microstructure, DAS, and hardness.

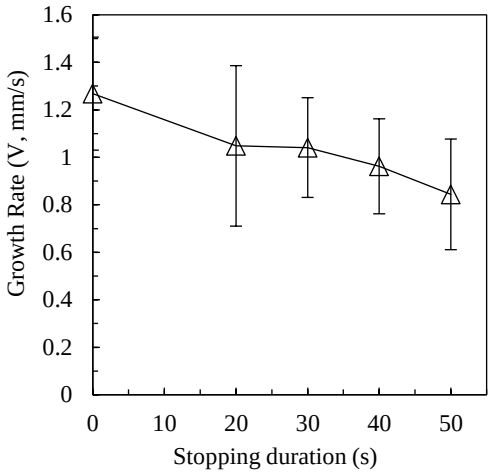

Figure 4. Relationship between growth rate and stopping duration

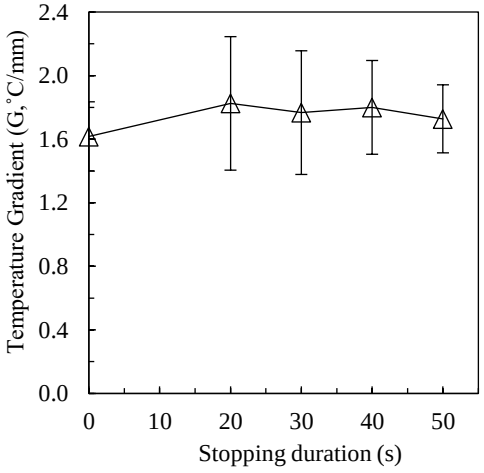

Figure 5. Relationship between temperature gradient and stopping duration

3.2. **Effects of Withdrawal Stop Duration on Microstructure**

Figure 6a-e shows the microstructure of the columnar dendrites and the directionally solidified DAS on the longitudinal section in different stopping durations. The microstructure on the transverse section in each stopping duration is shown in Figure 7a-e. The results show that α-Al dendrites became coarser and that their shapes changed from thin to round or oval when the stopping duration was increased. As can be seen in Figure 6a, the PDAS was very close and the SDAS was fine. In contrast, the SDAS was wide when the withdrawal stop duration of 50 s was applied (see in Figure 6e). In addition, the equiaxed columnar dendrites on the transverse section grew longer when the stopping duration rose (see in Figure 7). Withdrawal stop duration decelerated the solute growth, allowing diffusion in the liquid, which in turn tended to enlarge the SDAS. The SDAS was controlled by a coarsening process. Under this condition, some dendrites disappeared or merged together, resulting in increases in the spacing between arms. This promoted growth of dendrite branches. This is the main mechanism to promote α-Al dendrites coarseness. Furthermore, the different sizes of dendrites were linked to growth rate and cooling rate. Higher growth and cooling rates provided smaller dendrite arms. Thus, stopping duration influenced the solute-rich liquid distribution and in turn the microstructure.

3.3. **Effects of Withdrawal Stop Duration on Microstructure Parameters**

Figure 8 shows variations of PDAS and SDAS with stopping duration. The results showed that DAS and SDAS increased dramatically from 106.4 to 205.7 μm and 19.4 to 38.1 μm, respectively, when the stopping duration rose from 0 s to 50 s. Several factors affecting PDAS and SDAS were temperature gradient, growth rate, and cooling rate. Dendrite transformation was linked to temperature gradient and growth rate . PDAS appeared to be linked to solidification parameters, and SDAS was controlled by solidification time. Withdrawal stop duration allowed for freezing time, causing the growth rate to be slow. As documented in, while the temperature gradient increased, the growth rate remained constant. Under this condition, the PDAS and SDAS values became reduced. In contrast, while the growth rate increased, the temperature gradient remained constant. The PDAS and SDAS values decreased. According to the results of the present work, both PDAS and SDAS increased when the growth rate decreased, whereas the temperature gradient remained constant. Thus, the present work is in agreement with the previous report.

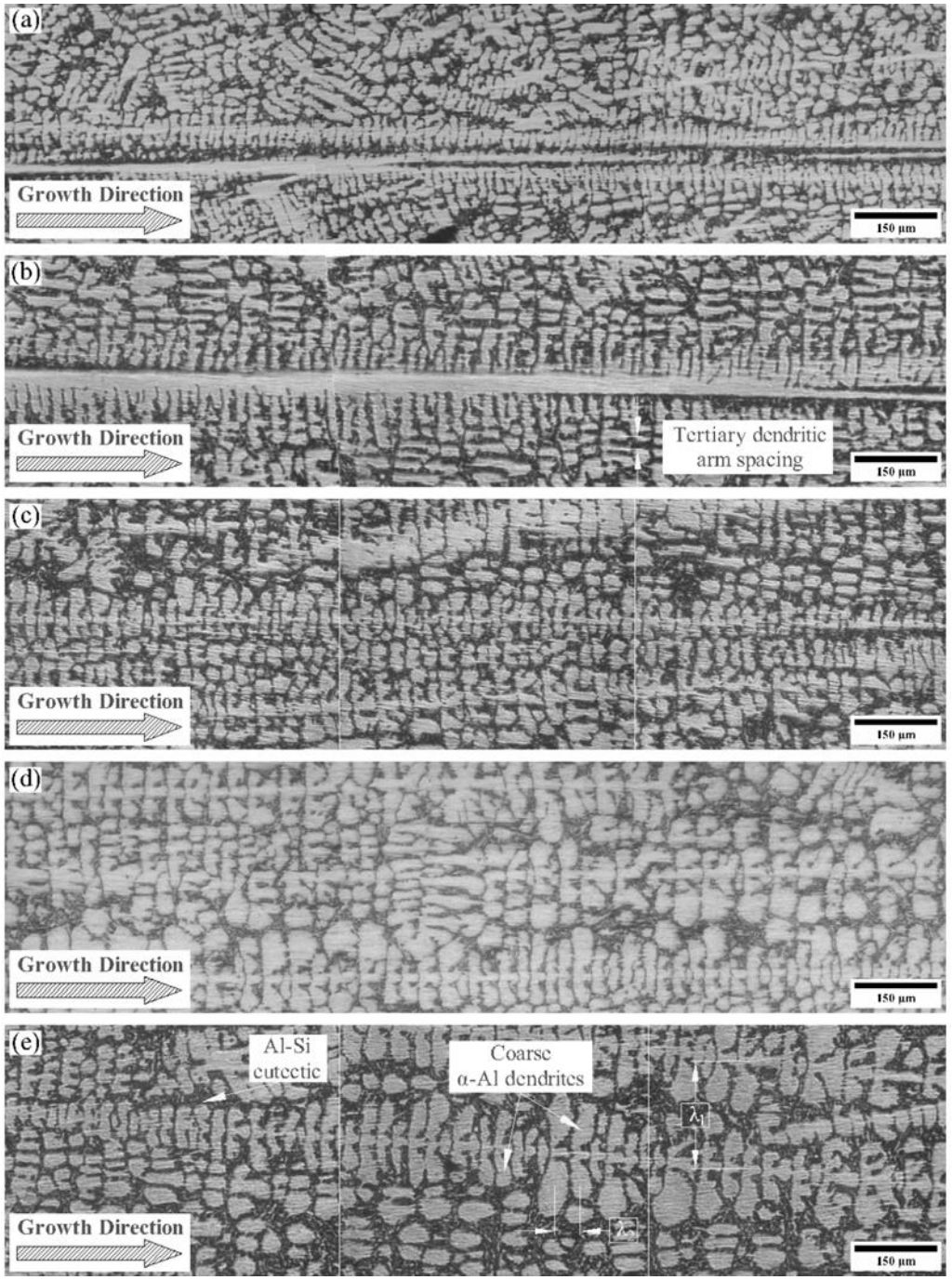

Figure 6. Microstructure on the longitudinal section in stopping durations: (a) 0 s; (b) 20 s; (c) 30 s; (d) 40 s; and (e) 50 s

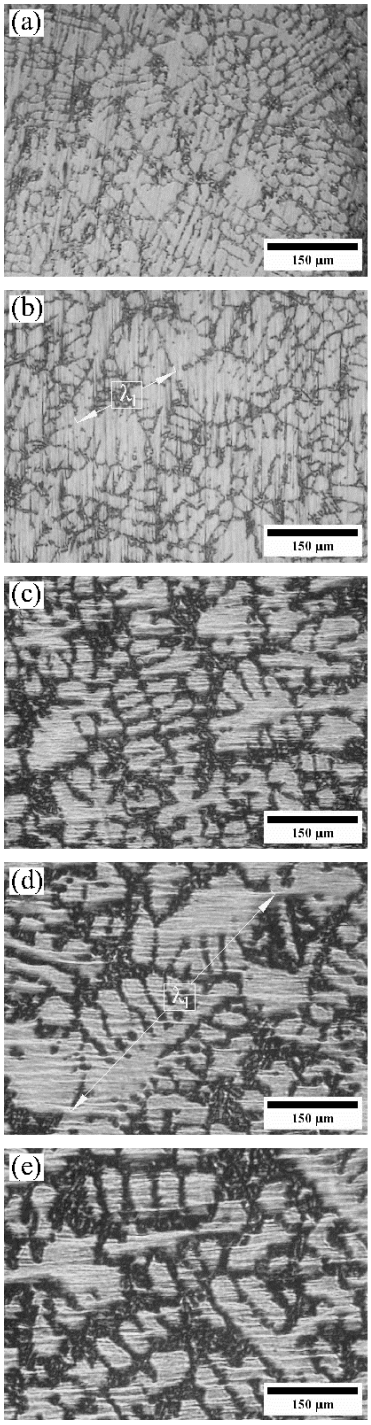

Figure 7. Microstructure on the transverse section in stopping durations: (a) 0 s; (b) 20 s; (c) 30 s; (d) 40 s; and (e) 50 s

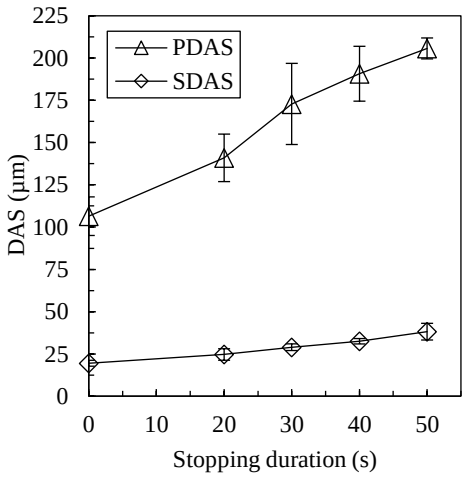

Figure 8. Relationship of PDAS and SDAS to stopping duration

3.4. **Effects of Withdrawal Duration on Microhardness**

Variation of microhardness values with stopping duration is shown in Figure 9. According to the results, microhardness decreased slightly when the withdrawal stop duration increased. When the stopping duration was extended from 0 s to 50 s, the hardness value was reduced from 54.0 to 49.9 HV. In general, microhardness depends on microstructure features like lamellar spacing or grain size: the finer the DAS, the better the mechanical properties, or the smaller the laminar spacing, the higher the hardness. Larger grain or dendrite sizes provide lower bonding forces between atoms because of easier atoms dislocation. This means that smaller grains or dendrite arms have greater ratios of surface area to volume and lead to greater obstacles to dislocation.

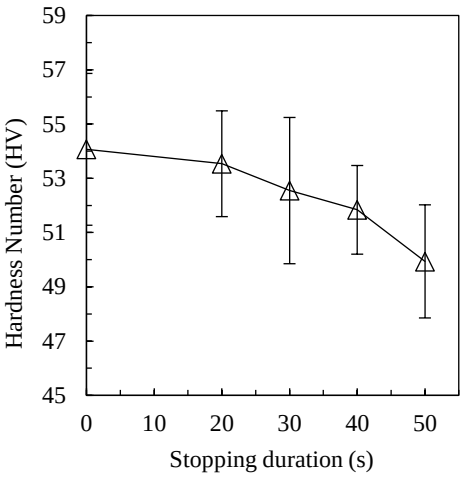

Figure 9. Variation of hardness value with stopping duration

3.5. **Relationships between Growth Rate, Microhardness, and Dendrite Arm Spacing**

Figure 10 shows the relationship between DAS and hardness, Figure 11 shows the relationship between growth rate and hardness, and Figure 12 .shows the relationship between growth rate and DAS. Those figures were obtained when the withdrawal stop duration was varied from 0 s to 50 s at constant temperature gradient of 1.74 ˚C/mm. As can be seen in Figure 10, hardness fell slightly when DAS increased. The highest hardness value of 54.0 HV was achieved when the PDAS achieved a minimum of 106.4 μm and SDAS achieved a minimum of 19.4 μm. Furthermore, hardness increased with the increase in growth rate (see in Figure 11). In addition, while the growth rate raised, the DAS declined steeply. The smallest values of PDAS and SDAS were found at the maximum growth rate of 1.26 mm/s (see in Figure 12). On the other hand, the largest PDAS value of 205.7 μm and the largest SDAS value of 38.1 μm where obtained when the growth rate was at its minimum (0.84 mm/s). Thus, mechanical properties can be improved by making the DAS finer. As reported in and increases in solidification parameters led to increases in microhardness. Not only hardness but also ultimate strength, ductility, and elongation fell when DAS increased. It was revealed that microstructure varied with growth rate. If the growth rate was high, the microstructure became finer. Moreover, microstructure failed to achieve accuracy uni-directionally if dendrites grew fast.

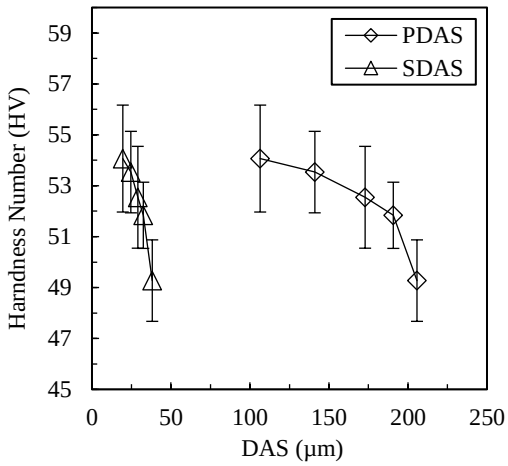

Figure 10. Relationship between hardness and DAS

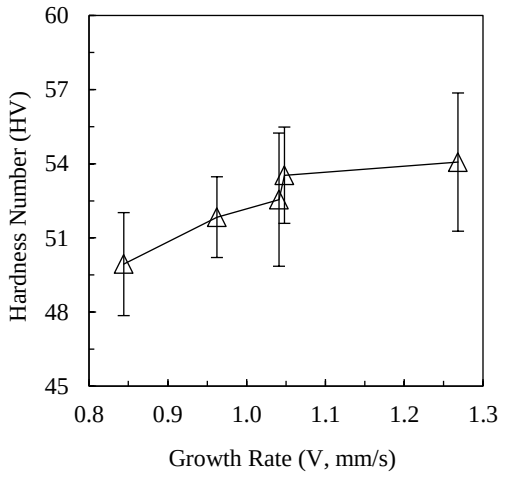

Figure 11. Relationship between growth rate and hardness

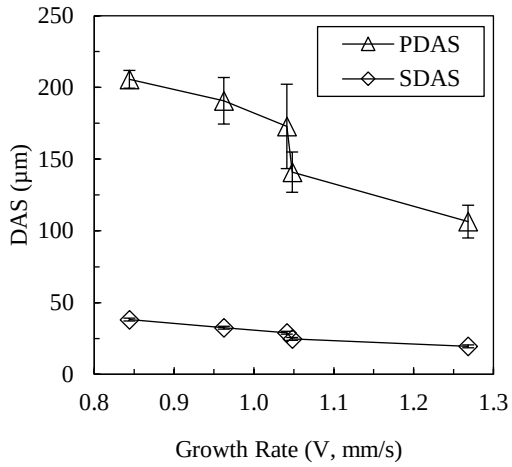

Figure 12. Relationship between growth rate and DAS

4. Conclusion

In this work, we experimentally examined the effects of withdrawal stop duration in the directional solidification of Al-7 wt% Si alloy on solidification parameters, microstructure, and microhardness. The following conclusions can be drawn from the experimental results. When the withdrawal stop duration was extended from 0 s to 50 s:

- the solidification parameter growth rate decreased slightly from 1.26 to 0.84 mm/s, while the solidification parameter temperature gradient was constant at 1.71 °C/mm,
- the microstructures of α-Al dendrites became coarser, and their shapes changed from thin to irregular plates; the values of primary and secondary dendrite arm spacings increased from 106.4 to 205.7 μm and 19.4 to 38.1 μm, respectively, and
- the microhardness value decreased from 54.0 to 49.9 HV.

5. Acknowledgments

This work was supported by the KNB Dikti scholarship program. The authors are grateful to KNB Dikti for the financial support.

6. References

D. M. Stefanescu, Science and engineering of casting solidification, Third Edit. SpringerInternational Publishing Switzerland 2015, 2009.

F. C. Robles-Hernandez, J. M. H. Ramírez, and R. Mackay, Al-Si Alloys. 2017.

H. Kaya and A. Aker, "Effect of alloying elements and growth rates on microstruture and mechanical properties in the directionally solidified Al-Si-X alloys," J. Alloys Compd., vol. 694, pp. 145–154, 2017.

H. Kaya, E. Çadirli, and M. Gündüz, "Dendritic growth in an aluminum-silicon alloy," J. Mater. Eng. Perform., vol. 16, no. 1, pp. 12–21, 2007.

H. Kaya, E. Çadirli, M. Gündüz, and A. Ülgen, "Effect of the temperature gradient, growth rate, and the interflake spacing on the microhardness in the directionally solidified Al-Si eutectic alloy," J. Mater. Eng. Perform., vol. 12, no. 5, pp. 544–551, 2003.

H. Zhong et al., "Effect of interdendritic thermoelectric magnetic convection on evolution of tertiary dendrite during directional solidification," J. Cryst. Growth, vol. 439, pp. 66–73, 2016.

J. Campbell, Complete Casting, First edit. Elsevier, 2011.

J. G. Kaufman and E. L. Rooy, Aluminum Alloy Castings: Properties , Processes , and Applications. 2004.

J. R. Davis, "Aluminum and Aluminum Alloys," in ASM International, 2001, pp. 351–416.

K. G. Basavakumar, P. G. Mukunda, and M. Chakraborty, "Influence of grain refinement and modification on microstructure and mechanical properties of Al-7Si and Al-7Si-2.5Cu cast alloys," Mater. Charact., vol. 59, no. 3, pp. 283–289, 2008.

M. Gupta and S. Ling, "Microstructure and mechanical properties of hypo/hyper-eutectic Al-Si alloys synthesized using a near-net shape forming technique," J.

Alloys Compd., vol. 287, no. 1–2, pp. 284–294, 1999.

M. Okayasu and S. Takeuchi, "Crystallization characteristics of cast aluminum alloys during a unidirectional solidification process," Mater. Sci. Eng. A, vol. 633, pp. 112–120, 2015.

M. Şahin and E. Çadirli, "The effects of temperature gradient and growth rate on the microstructure of directionally solidified Sn-3.5Ag eutectic solder," J. Mater. Sci. Mater. Electron., vol. 23, no. 2, pp. 484–492, 2012.

N. Maraşli, K. Keşlioğlu, B. Arslan, H. Kaya, and E. Çadirli, "Effects of growth rate and temperature gradient on the microstructure parameters in the directionally solidified succinonitrile-7.5 wt.% carbon tetrabromide alloy," J. Mater. Process. Technol., vol. 202, no. 1–3, pp. 145–155, 2008.

S. Engin, U. Büyük, and N. Maraşli, "The effects of microstructure and growth rate on microhardness, tensile strength, and electrical resistivity for directionally solidified Al-Ni-Fe alloys," J. Alloys Compd., vol. 660, pp. 23–31, 2016.

S. Steinbach and L. Ratke, "The influence of fluid flow on the microstructure of directionally solidified AlSi-base alloys," Metall. Mater. Trans. A, vol. 38 A, no. 7, pp. 1388–1394, 2007.

U. Böyük, S. Engin, and N. Maraşli, "Microstructural characterization of unidirectional solidified eutectic Al-Si-Ni alloy," Mater. Charact., vol. 62, no. 9, pp. 844–851, 2011.

W. Rasband, "Downloads - ImageJ," 2018. [Online]. Available: https://imagej.net/Downloads. [Accessed: 12-Apr-2019].

Y. Kaygısız and N. Maraşlı, "Directional solidification of Al–Cu–Si–Mg quaternary eutectic alloy," J. Alloys Compd., vol. 721, pp. 764–771, 2017.

Y. Koçak, S. Engin, U. Böyük, and N. Maraşlı, "The influence of the growth rate on the eutectic spacings, undercoolings and microhardness of directional solidified bismuth–lead eutectic alloy," Curr. Appl. Phys., vol. 13, no. 3, pp. 587–593, 2013.

Journal of Materials Processing and Characterization (JMPC) is an international, open-access and peer-reviewed journal aimed to facilitate researchers in disseminating their research works in the field of processing and characterization of engineering materials as well as biomaterials for biomedical applications. The journal is published jointly by Department of Mechanical and Industrial Engineering, Faculty of Engineering, Universitas Gadjah Mada (UGM) and Centre for Innovation of Medical Equipment and Devices (CIMEDs) UGM.

In general, JMPC covers all the research topics related to the processing (such as material preparations, fabrication techniques, post-processing treatments) and characterizations (such as novel methods for characterization, experimental testing and numerical analyses) of metals, polymers, ceramics and composites. To be more specific, the journal covers the following research topics:

1. Processing technologies of engineering materials and biomaterials, including casting, solidification, forming, forging, hot and cold-working, machining, powder metallurgy, extrusion, heat treatments, additive manufacturing, welding, and injection moulding.
2. Surface treatments of engineering materials and biomaterials, including coatings, shot and grit blasting, anodization, physical and chemical treatments.
3. Characterizations of engineering materials and biomaterials, including microstructural analysis, surface characterizations, mechanical testing, electrochemical characterization and tribological testing.
4. Failures of engineering materials and biomaterials, including fractures, fatigue, corrosion and wear.

We cordially invite authors to submit their manuscript in English and in the form of either research articles or review papers.

JMPC is now open access

All issues of JMPC are now available to read online, free of charge. Articles are also free to download and share in accordance with the Creative Commons Attribution-ShareAlike 4.0 International license. Visit the website at https://jurnal.ugm.ac.id/jmpc to read this or any past issue online.

ONLINE SUBMISSIONS

Have a Username/Password for Journal of Materials Processing and Characterization.

Registration and login are required to submit items online and to check the status of current submissions.


9 772716 128002

9 772714 972003